

AFRL-OSR-VA-TR-2013-0056

Fundamental Physics and Engineering of Nanosecond-Pulsed Nonequilibrium Microplasma in Liquid Phase without Bubbles

ALEXANDER FRIDMAN

DREXEL UNIVERSITY

01/04/2013
Final Report

DISTRIBUTION A: Distribution approved for public release.

AIR FORCE RESEARCH LABORATORY
AF OFFICE OF SCIENTIFIC RESEARCH (AFOSR)/RSE
ARLINGTON, VIRGINIA 22203
AIR FORCE MATERIEL COMMAND

REPORT DOCUMENTATION PAGE

Form Approved
OMB No. 0704-0188

The public reporting burden for this collection of information is estimated to average 1 hour per response, including the time for reviewing instructions, searching existing data sources, gathering and maintaining the data needed, and completing and reviewing the collection of information. Send comments regarding this burden estimate or any other aspect of this collection of information, including suggestions for reducing the burden, to the Department of Defense, Executive Services and Communications Directorate (0704-0188). Respondents should be aware that notwithstanding any other provision of law, no person shall be subject to any penalty for failing to comply with a collection of information if it does not display a currently valid OMB control number.

PLEASE DO NOT RETURN YOUR FORM TO THE ABOVE ORGANIZATION.

1. REPORT DATE *(DD-MM-YYYY)*	2. REPORT TYPE	3. DATES COVERED *(From - To)*
29-12-2012	FINAL	30 Sept 11 - 29 Sept 12

4. TITLE AND SUBTITLE

Fundamental Physics and Engineering of Nanosecond-Pulsed Nonequilibrium Microplasma in Liquid Phase without Bubbles

5a. CONTRACT NUMBER

5b. GRANT NUMBER

FA9550-11-1-0280

5c. PROGRAM ELEMENT NUMBER

6. AUTHOR(S)

A. Fridman (PI), D. Dobrynin, G. Friedman, G. Fridman, Y. Cho, M. Pekker, M. Shneider

5d. PROJECT NUMBER

5e. TASK NUMBER

5f. WORK UNIT NUMBER

7. PERFORMING ORGANIZATION NAME(S) AND ADDRESS(ES)

Drexel University
3141 Chestnut St
Philadelphia PA 19104

8. PERFORMING ORGANIZATION REPORT NUMBER

9. SPONSORING/MONITORING AGENCY NAME(S) AND ADDRESS(ES)

AF Office of Scientific Research
875 N Randolph St Room 3112
Arlington VA 22203

10. SPONSOR/MONITOR'S ACRONYM(S)

11. SPONSOR/MONITOR'S REPORT NUMBER(S)

AFRL-OSR-VA-TR-2013-0056

12. DISTRIBUTION/AVAILABILITY STATEMENT

DISTRIBUTION A: APPROVED FOR PUBLIC RELEASEDS

13. SUPPLEMENTARY NOTES

14. ABSTRACT

The team has demonstrated the possibility of formation of non-equilibrium microscale plasma in the liquid phase and studied the dynamics of excitation and quenching of non-equilibrium MPD in liquid water: the dynamics of the high-voltage nanosecond and subnanosecond pulsed discharge in water without bubbles was investigated; liquid plasma generation without formation of gas bubbles was demonstrated; up to 5000 km/s propagation velocity was observed for a subnanosecond discharge; electron densities and temperatures were measured; a mechanisms of nanosecond discharge development in liquid phase was developed. It was shown that liquid phase plasma is not limited to water in which it has been first observed, but may be generated in virtually any liquid. It was shown that conventional Townsend and streamer breakdown mechanisms are limited in liquid by short electron mean-free path and consequently not sufficient mean electron energy. Quasi-homogeneous generation of liquid phase plasma by nano- and subnanosecond high voltage pulses can be attributed to a cold leader-type mechanism that is similar to generation and propagation of

15. SUBJECT TERMS

16. SECURITY CLASSIFICATION OF:			17. LIMITATION OF ABSTRACT	18. NUMBER OF PAGES	19a. NAME OF RESPONSIBLE PERSON
a. REPORT	b. ABSTRACT	c. THIS PAGE			Alexander Fridman
U	U	U	U	43	19b. TELEPHONE NUMBER *(Include area code)* 215.895.1542

Reset

Standard Form 298 (Rev. 8/98)
Prescribed by ANSI Std. Z39.18

Final Performance Report

Fundamental Physics and Engineering of Nanosecond-Pulsed Nonequilibrium Microplasma in Liquid Phase without Bubbles

Drexel Plasma Institute, Drexel University

in collaboration with Princeton University

PI: Alexander Fridman

Table of contents

1. Introduction....3
2. Tasks and deliverables....5
3. Experimental setup....6
4. Detailed report by tasks....10
    - Task 1. Experiments investigating dielectric properties of the liquid....10
    - Task 2. Registration of high energy emission....16
    - Task 3. Plasma diagnostics using optical emission spectroscopy....19
    - Task 4. Effects of electrode size and material and externally applied electric and magnetic fields....24
    - Task 5. Development of the discharge model....30
5. Discussion and conclusions....37
6. Publications and conference proceedings....40
7. References....41

1. Introduction

Studies investigating discharges in liquids have been performed for many decades, as in the work reviewed by Joshi *et al.* [8], Bruggeman and Leys [5], and Graham and Stalder [1]. From these reviews substantial evidence exists in support of the "bubble mechanism" to describe the initiation and development of discharges in water. More recently, our group reported experimental results showing the possibility of producing discharges directly in water without any void/bubble formation. Work by Stuve [13] also argued for direct field ionization of water molecules under the application of strong non-uniform electric fields. These in turn gave support for the "direct ionization mechanism", the main competing theory against the bubble theory. To this day, the dispute between both theorems still exists, and often the choice of which is applicable is based on a particular experimental setup.

The major problem hindering the formation of plasma in liquids is the low mean free path and high scattering rates experienced by electrons moving through the liquid [8]. Particularly for water, electrons are also known to be quickly solvated and hence have a very short lifetime. The mean free path λ, of a particle in a fluid is related to the number density of collisional partners, n, and the collision cross section, σ given by: $\lambda = 1/n\sigma$. For liquids, the density of collision partners is 1000 times greater than that of gases. Thus simple estimates show that the mean free path decreases by almost 3 orders of magnitude for free electrons in liquids than in a gas at atmospheric pressure. Furthermore, the values for σ calculated for gases do not scale with density for liquids, as these values are based on binary collisional models, and multi-particle interactions in liquids cannot be ignored.

This reduction in mean free path means that at applied electric fields close to the breakdown criterion of gases, most electrons lose their energy in collisions before gaining enough to cause ionization. To compensate for the decrease in mean free path, a corresponding electric field intensity increase by 3 orders of magnitude should be enough to promote direct ionization in a liquid. This qualitative assessment is a restatement of the prediction made by the Paschen curve, and so one would expect roughly $30MV\ cm^{-1}$ breakdown electric field for liquids.

Yet still, field intensities only slightly higher than those for gases have been shown to initiate discharge in liquids. Physicists attributed the bubble mechanism to explain this observed phenomenon. Under high electrical stress, liquids and the electrode-liquid interface can undergo many different electrochemical reactions. Electrolysis, Joule heating, electrostatic expansion of pre-existing micro-voids, and molecular decomposition can all lead to the formation of low density regions near the electrode. Within these low density regions, the mean free path is now

much longer, and electrons can gain enough energy being accelerated inside these voids to cause ionization [6]. The size of the required bubble depends on the nature of the liquid, the applied external electric field, and the local electric field near the point of nucleation. Associated with this mechanism are electrical measurements which reveal a steady flow of current, characteristic of liquid heating due to molecular and ion movement near the electrodes. This low initial current stage has been correlated to vapour region growth through the use of shadow imaging [6, 8, 11], verifying a dedicated initiation mechanism.

Direct ionization in the other hand is implied when discharge phenomenon is observed on nanosecond and sub-nanosecond time scales from the onset of overvoltage. The typical times for the formation of voids of the right sizes to support avalanche formation is on the order of microseconds for a 40kV pulse of rise time 20ns [6, 11]. Discharges which form in 0.5 to $1ns$ therefore indicate a clearly different mechanism of ionization, one capable of producing enough charge accumulation to expel streamers into dense media. Since significant bubble formation is typically non-existent on this time scale, the only other explanation is direct ionization due to the field or electron impact.

2. Tasks and deliverables

Task #	Task	Deliverables
1	Generation of the discharge in liquids with different polarization and dielectric properties to study the hypothesis related to the polarization mechanism.	*Experimental data on plasma generation parameters as a function of polarization and dielectric properties of liquid in which plasma is ignited*
2	Registration of the discharge emission in the high energy range of spectra	*Experimental data on plasma emission in the high-energy range of spactra*
3	Spatially and temporally resolved registration of the discharge emission to determine basic plasma characteristics	*Experimental data on basic plasma parameters obtained from spatially and temporally resolved plasma emission*
4	Study the effects of electrode materials and sizes, electrode gap, effect of external electric and magnetic fields on the discharge development and characteristics	*Experimental data on plasma generation parameters as a function of electrode material, discharge gap, external electric and magnetic fields*
5	Development of model of the discharge based on proposed hypotheses, and comparison with the results of experimental studies	*Models and data on plasma parameters and characteristics, and results of analytical comparison with experimental data*

3. Experimental setup

In the study we have used similar setup described in [10]. The discharges produced in these experiments were generated via a point-to-plane electrode setup. The discharge cell had a point-to-plate geometry with the high-voltage electrode being either stain-less steel needle with diameter of 20 μm, or a 50 mm long, 100 μm diameter Iridium needle, with an electrochemically etched tip of radius of curvature 1–1.5μm (IR20030.1A4, MicroProbes for Life Sciences). The entire needle was insulated using a Teflon encasement and epoxy, except for the last 2 mm which was acted as the effective submerged anode. The inter-electrode distance was varied in the range of 1.5-4 mm. The liquid layer between the center of the discharge gap and quartz window was 50 mm. In order to study the effect of polarizibility and dielectric properties of liquid on the discharge development we used two types of liquids in the experiments described below: distilled deionized (Type II) water (EMD Chemicals), and polydimethylsiloxane (C2H6OSi)n transformer oil (dielectric constant ε = 2.3-2.8). The cathode was an 18mm diameter copper plate, and the electrode gap varied from 1.3 to 6.5mm. The discharge cell was fitted with 1mm thick quartz windows to allow imaging of the discharge gap, and the entire chamber contained roughly 50 ml of liquid when filled – see Figure 1. The liquid surface was left open to the air, subject to atmospheric pressure.

Nanosecond pulse generators from FIDTechnology were used to produce high-voltage pulses +11.2 to +15.5kV in amplitude. The pulses had a 2ns rise time (10 – 90%) and 10ns duration, with a fall time of 3ns; details of these characteristics were supplied by the manufacturer (FiDTech). Pulses were delivered to the electrodes over 50ft of RG 393/U coaxial cable, the long cable length necessary to isolate reflected pulses. A back current shunt (BCS) consisting of 12 low-inductance 3Ω resistors soldered into the cable shielding was mounted midway through the length of the cable, the design of which is discussed in further detail in [15]. This enabled waveform monitoring for synchronization purposes, and the digital oscilloscope trace of the typical incident pulse is shown in Figure 2. Open circuit reflection measurements indicated a 28.5ns signal delay time from the BCS to the discharge chamber electrodes. The internal delay of the power supply operating in externally triggered mode was approximately 20.5μs, with a constant drift of -0.2μs after about 2 hours of constant operation. This relatively large uncertainty in the power supply output timing was mitigated by constantly monitoring the BCS signals which included the power supply delays.

The emission stage of the discharge was observed using fast photography enabled by the 4-Picos ICCD[1] camera from Stanford Computer Electronics. This camera has an 18mm diameter multi-alkaline photocathode with a spectral response from 180-750 nm, and an internal trigger-

[1] Intensified Charge Coupled Device

propagation delay of 63.5ns to the gating of the MCP[2] (0.5ns jitter). Image capture synchronization with the incident voltage pulse on the electrodes was achieved by carefully monitoring the camera gate strobe signal and the HV cable BCS signal, with consideration of the appropriate trigger propagation and line delays.

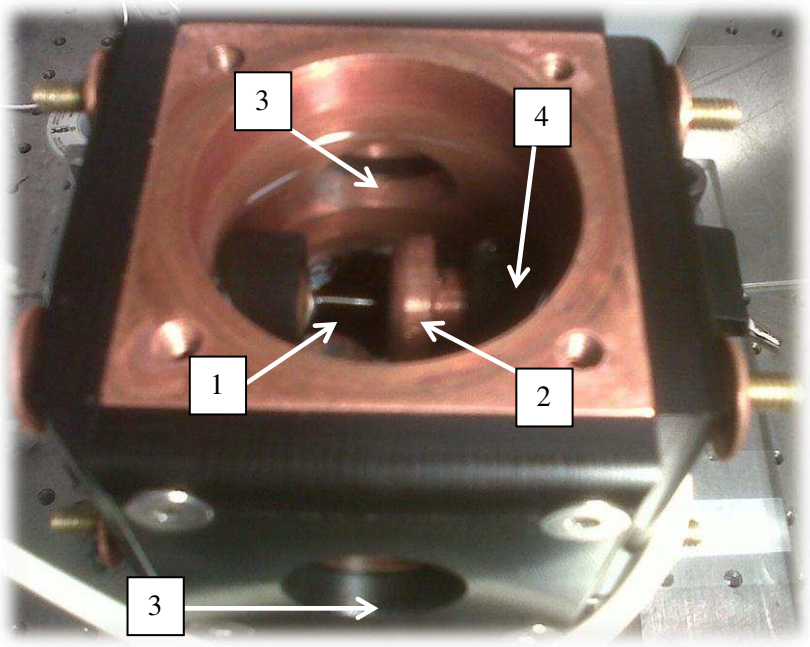


Figure 1: Discharge cell for nanosecond in liquid experiments.
(1) - Anode; (2) - Cathode; (3) - Quartz viewing windows; (4) - Electrode insulation from chamber.

[2] Micro Channel Plate

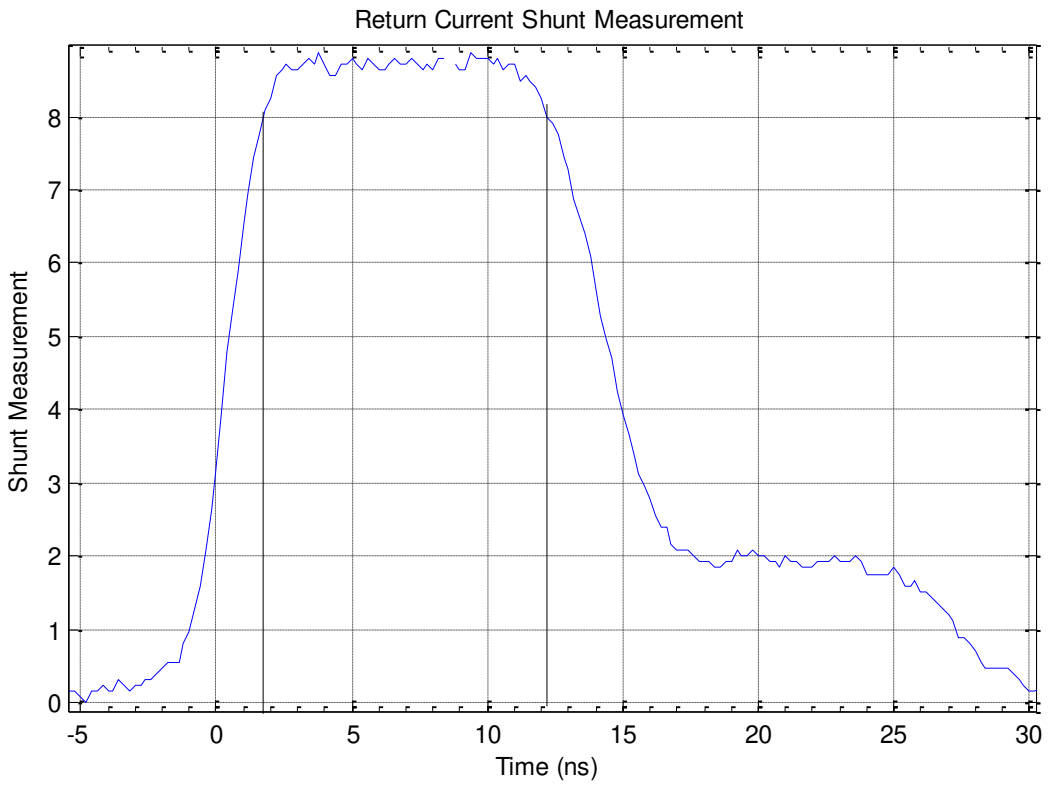


Figure 2: Back current shunt measurement of incident pulse generated by nanosecond pulse power supply

Synchronization of the discharge with the camera shutter was controlled using the camera's internal programmable delays, in conjunction with a dual-channel Arbitrary Function Generator (AFG3252, Tektronix). The synchro-output of the generator's two adjustable channels produced triggering signals with a rise/fall time less than 2.5ns. These pulses were used to trigger both the camera shutter and the power supply with a typical jitter less than 20ps.

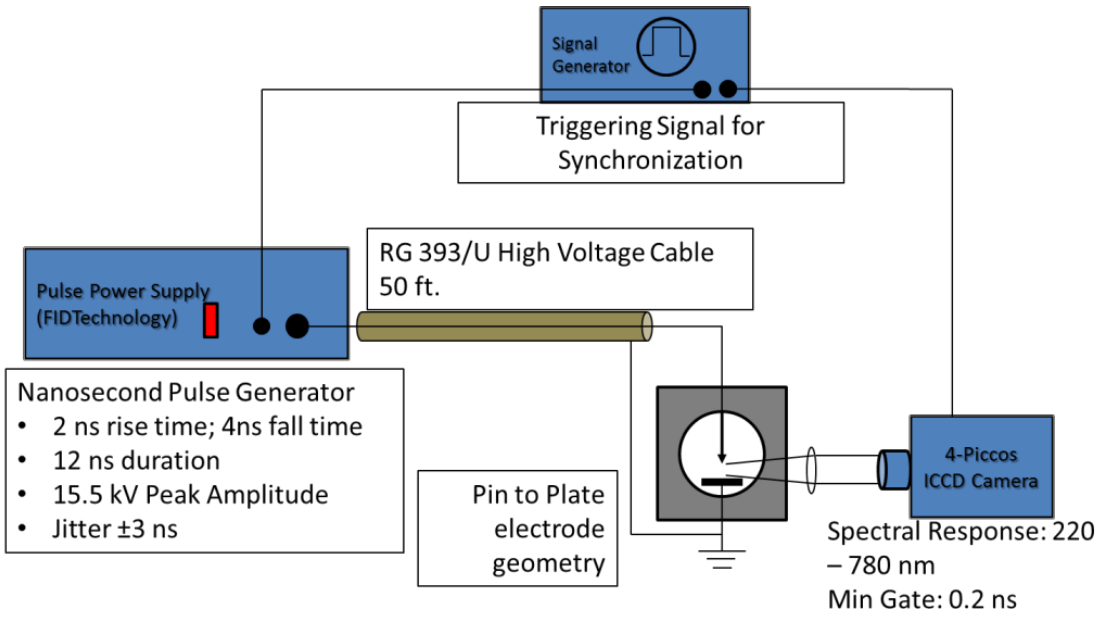


Figure 3: Schematic of basic experimental setup.

Shadow imaging was also performed over various stages throughout the discharge development, with a 650nm, 5mW laser diode supplying a collimated light source for backlighting. This setup allowed any density inhomogeneity of $\sim 1 \mu m$ in the liquid to be detected, and thus the presence of any bubbles of voids comparable to the size of the emitting channels would be revealed.

Optical emission spectroscopy of the discharge emission was facilitated by a Princeton Instruments, TriVista spectrometer (Acton-Research, TriVista TR555), coupled to a Roper Scientific digital ICCD detector (Acton-Research, SpectrumM). Fiberoptic coupling of the light from the discharge to the spectrometer system was done using a 10-fiber Princeton Instruments fiberoptic bundle, with a $200 \mu m$ single-core diameter. These results were necessary to determine the nature of the emitting species.

Finally, voltage and current measurements to characterize the electrical behaviour of the discharge loading were performed. Voltage measurements were based on BCS waveform analysis combined with manufacturer data for the power supply setting. Current measurements were made using a Pearson Current Monitor (Model 6586), having a useable rise time of 1.5ns, and a sensitivity of $0.5 V A^{-1}$ into 50Ω cable. Transmission line analysis was used to determine the voltage and current behaviour of the discharge based on line delays and pulse reflections.

4. Detailed report by tasks

Task 1. Experiments investigating dielectric properties of the liquid

One attempt to explain discharge formation directly in water without any indication of bubble initiation considers electric field enhancement associated with water molecules. This ubiquitous liquid, water, has some very unique properties, including a large dielectric constant ($\epsilon_r \approx 80$) and hence a very high molecular polarizability. The strong dipoles in the water molecules provide electric field enhancement leading to significant local electric field enhancement near the electrode tip [Stuve 2012]. The magnitudes of these fields are close to the predicted breakdown electric fields for liquid estimated by the Paschen curve: $30\ MV\ cm^{-1}$ [Fridman 2012], even with the application of much lower globally applied voltages. A field ionization mechanism therefore would cause the discharge to develop on a sub-nanosecond timescale since molecular reorientation occurs on picosecond timescales. If dielectric properties indeed played a significant role in this mechanism, such rapid discharge formation would not be possible in a medium with low polarizability and small dielectric constant where field enhancement is significantly lower. In long chain polymer liquids, high electric fields have been shown to influence molecular re-orientation; however, field dissociation and ionization require electric fields on the order of $10^2 MV\ cm^{-1}$ ($\sim 200 MV\ cm^{-1}$for ethylene glycol) [Kreuzer 2004], much lower than the electric fields under study in these experiments.

This section reports on the experimental findings associated with initiation of discharges in liquids with low dielectric constant. Nanosecond pulsed discharges are ignited in polydimethylsiloxane (PDMS), also known as silicone oil. The decision to use this liquid was due to several factors, chief amongst them being the medium's low polarizability and hence a low dielectric constant ($\epsilon_r = 1.8$). These dielectric properties of PDMS are commonly exploited in applications for high-voltage electrical insulation, where it finds use as an arc-suppressant for transformers and high-voltage switches. Additionally, the optical transparency would allow easy observation of the emission phase. Finally, the non-volatile and non-toxic nature of the liquid made handling and experiments less complicated. Some work was also performed in liquid hexane – having a much lower molecular weight, but comparable dielectric strength to PDMS.

Existence of the discharge in non-polar liquid

The first major result to be reported was the existence of the discharge in non-polar liquid media – figure 4 below shows an ICCD image taken in PDMS. The exposure time of the camera gate was 20ns, and the cropped image shown in Figure 4 (a) is approximately $0.5mm \times 1mm$. This image represents the emission observed due to a single incident pulse to the electrodes. The camera gate was triggered to encompass the entire duration of the incident voltage pulse to the electrodes, including the rising edge, plateau and falling edge of the pulse – see Figure 4 (b). A $32kV$ applied electric field on the electrode gap was used, with approximately 3mm separation between electrodes.

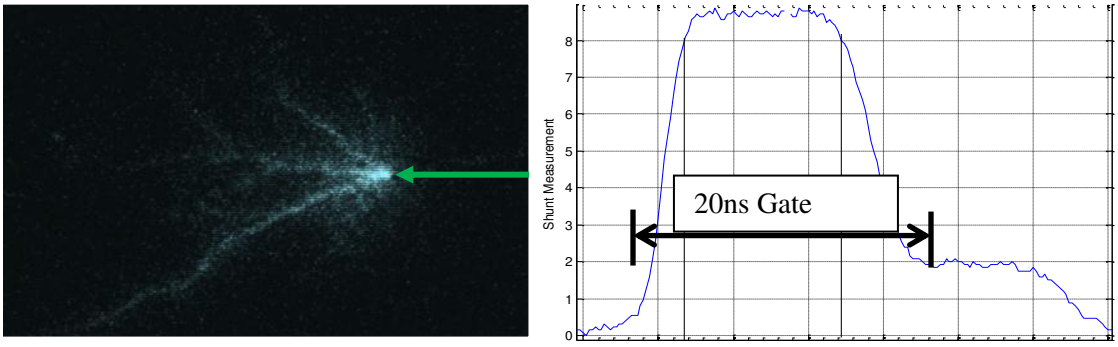


Figure 4: (a) Left – Discharge in PDMS, 0.5 x 1mm. Green arrow shows anode tip position;
(b) Right – Camera gate over incident voltage pulse

Delay time to initiation was $1 - 2ns$, the error associated with uncertainty in the internal delay of camera electronic shutter ($34 - 35ns$ from trigger). Such a short discharge initiation time presents initial evidence for the absence of the bubble initiation, with arguments that time required for bubble to grow is $\gg 2ns$. Subsequent analysis will show the required bubble size to ensure plasma generation.

Discharge development over time

To observe the discharge development over time, a much shorter camera gate had to be used. The maximum frame rate – as limited by the camera hardware – was 30fps. The applied voltage pulse as shown in Figure 2 lasts for no more than 20ns, and thus obtaining a series of images as close as 1ns apart required signal accumulation from successive pulses. This method relies heavily on the discharge having good reproducibility from pulse to pulse. Signal accumulation lead to a loss of information about the discharge structure, but a general idea about the discharge growth rate could be obtained.

In contrast to the emission intensity observed for discharges in water, the emission in PDMS was much weaker – see Figure 5. As a consequence, the short exposure times used demanded image accumulation to ensure an acceptable signal to noise ratio.

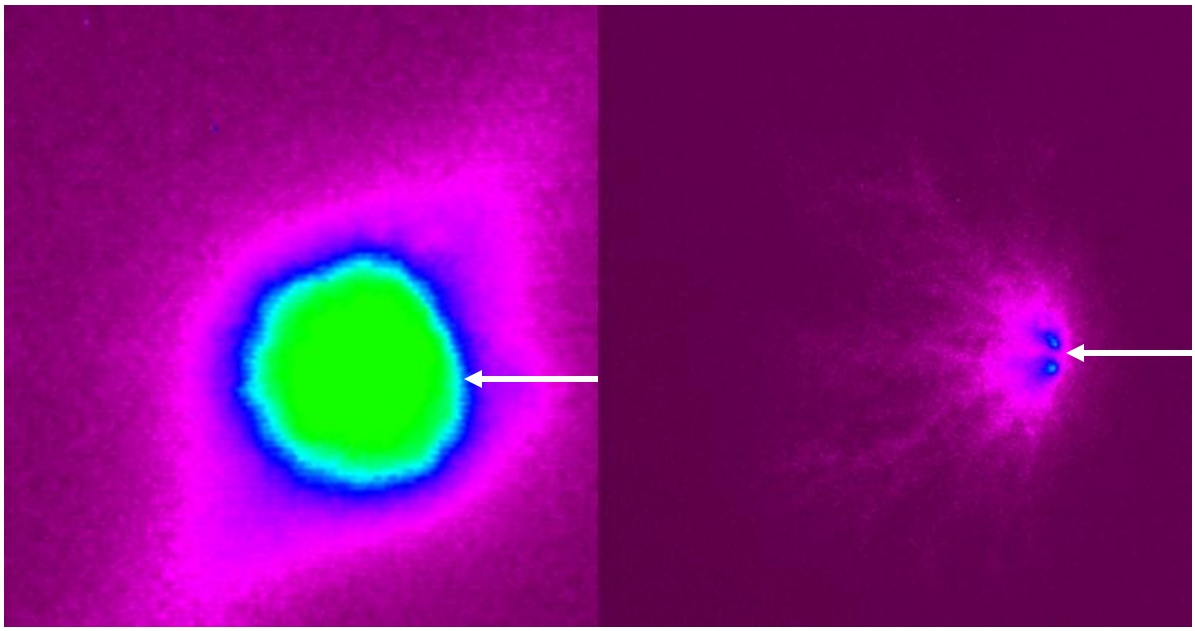


Figure 5: Discharge ignited in water (left) and PDMS (right) under the same conditions. Image Size 1 x 1mm. Applied voltage 15.5kV with 1.5mm electrode separation. Each image is an accumulation of 10 discharges.

The initial experiments were traced using 500ps exposures with 50 images accumulation, the results reproduced here in Figure 6. For PDMS, the weak emission intensity required accumulation of 10 images with a 2ns exposure. Furthermore, for experiments in hexane, the emission intensity was even weaker, requiring a 5ns exposure time to acquire an acceptable signal. The results are summarized in Figure 6 and Figure 7. The images are superimposed onto the waveform of the voltage pulse incident on the electrodes, at the time during the pulse when they were taken.

The results of the discharge in water show a pronounced dark phase during the pulse plateau – Figure 6. This was explained by the authors as charge separation and screening of the applied electric field leading to quenching of the emitting plasma. This quenching phase was also observed in both PDMS and hexane, although the effect was much less prominent. The longer exposure times used may have masked the existence of a complete dark phase as observed in water.

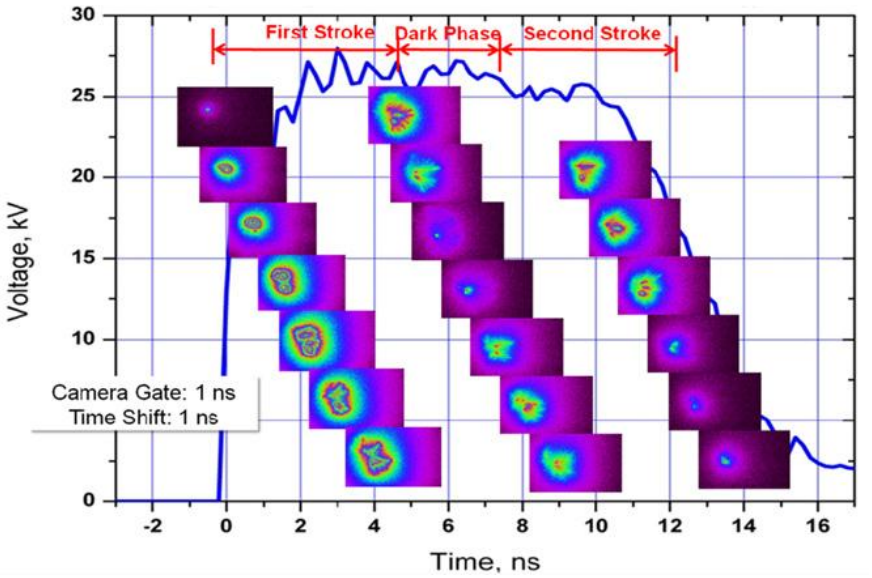


Figure 6: Development of nanosecond discharge in water.
Reproduced from Starikovskiy *et al* (2011).

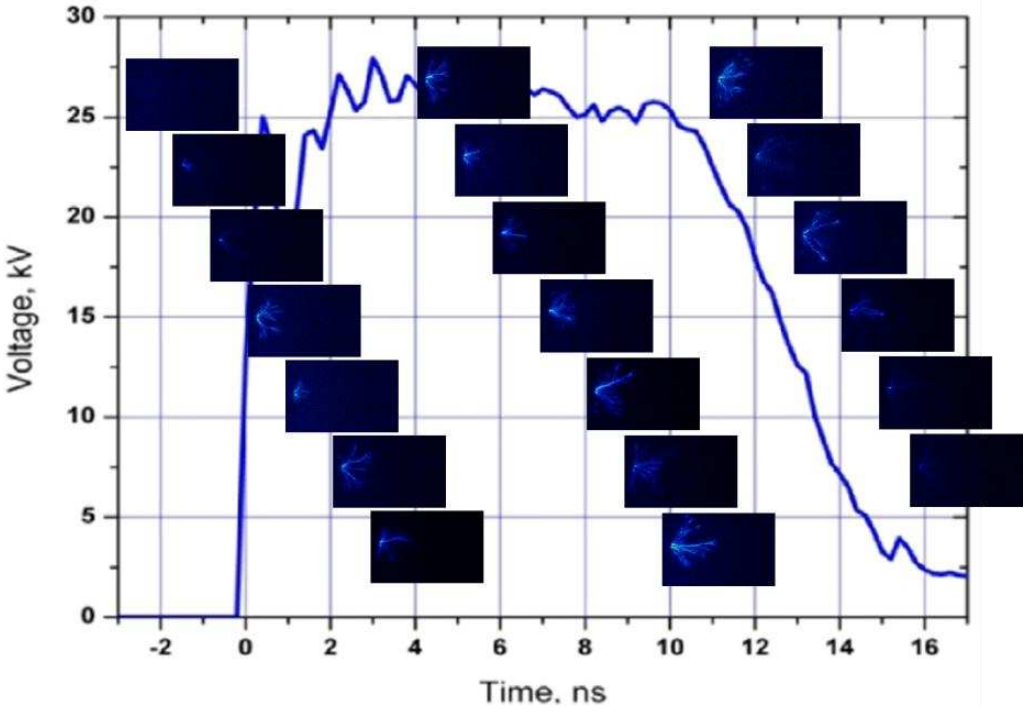


Figure 7: Development of discharge in PDMS. Images: 1ns Exposure, 1ns step.

Effect of electric field

The dependence of the discharge size on the applied field was also investigated for PDMS, hexane and water. Long exposure images for 20ns were taken to observe the full development of the discharge as a result of a single incident pulse. The timing diagram for the image acquisition was identical to that shown in Figure 4 (b).

The effective electric field was varied by changing the applied voltage to the electrodes, along with the electrode separation – for PDMS, water and hexane these results are tabulated in Figure 8, Figure 9, and Figure 10 shown below. At electrode separation higher than 1.5mm, no emission in hexane could be observed. It is important to note that the voltages labelled on the columns represent the applied voltage pulse amplitude. The actual peak voltage on the discharge gap has amplitude twice of that shown.

For the experiments in water, the discharge size appears to be independent of the separation of the electrodes, and more dependent on the applied voltage. This behaviour does is not obeyed by the other liquids investigated however, as there are notable differences for various electrode separation in PDMS. At 6.5mm and 3.5mm separation, the size of the emitting region in PDMS remains roughly the same, but when reduced to 1.3mm, the diameter of this emitting region almost doubles. Similar trends in hexane were difficult to obtain since the discharge was completely dark for electrode distances more than 1.5mm. At gap separation less than 0.5mm, a spark was formed in hexane.

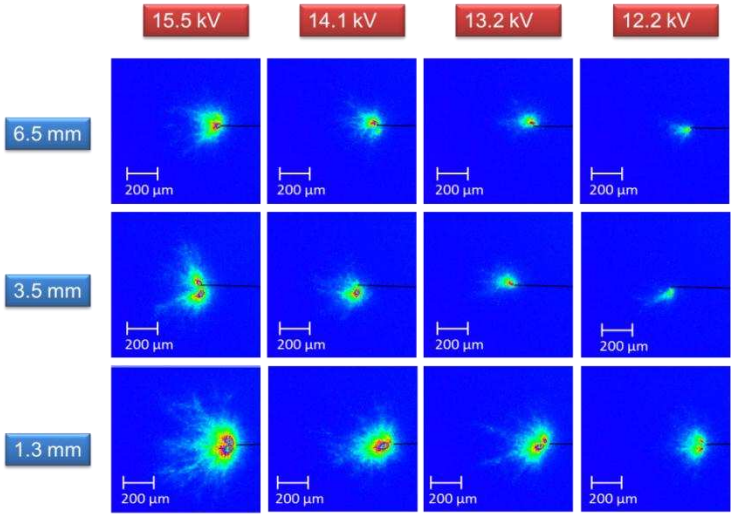


Figure 8: PDMS - Discharge size as a result of varying applied voltage (columns) and electrode separation (rows). Image: 20ns Exposure with 10 accumulation; Size: 1mm x 1mm.

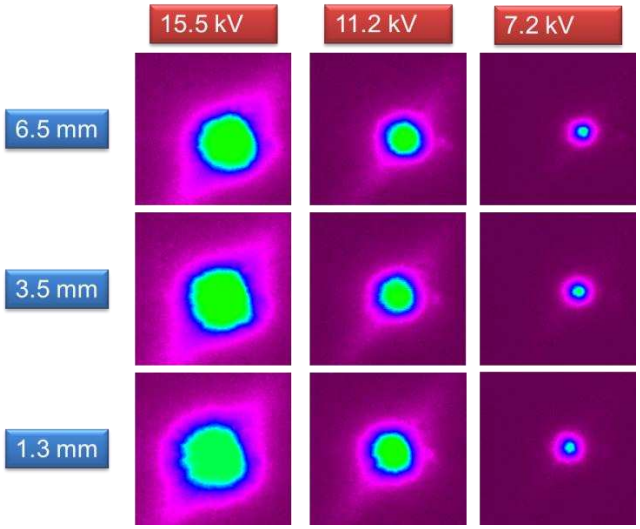


Figure 9: Water - Discharge size as a result of varying applied voltage (columns) and electrode separation (rows). Image: 20ns Exposure with 10 accumulation; Size: 1mm x 1mm.

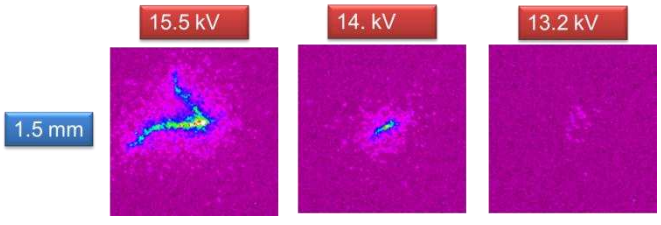


Figure 10: Hexane - Discharge size as a result of varying applied voltage (columns) and electrode separation (rows). Image: 20ns Exposure with 10 accumulation; Size: 0.5mm x 0.5mm

Task 2. Registration of high energy emission

Measurement of high energy emission was facilitated by the X-123 Spectrometer from Amptek. The CdTe detector had an optimal detection range from 5 to $150\ keV$. An uncalibrated device was available at the time of use, and thus quantitative determination of the energy detected could not be made. Estimates of the wavelengths detected were made based on specifications of the device given by the manufacturer. Experiments were performed for discharges ignited in water with the application of +15.5kV to the pin electrode across a 5mm gap and the anode was the 2μm Ir tip. Pulse repetition frequency was 10 Hz.

The major results of the experiments are shown in Figure 11 below. The detector was placed 1 cm away from the discharge region and data was acquired for 100s with the discharge on and off. Figure 11 shows the increase in high energy emission with the discharge turned on, both in the number of counts as well as the wavelength of the radiation. With the discharge turned on, the counter registered an order of magnitude increase in the detected high energy photons from 20 to 190 over the same period of time. These results were reproducible over several experiments, with the final pulse count after 100s varying from 150 to 200 counts. Estimates of the energy associated with the measured radiation were assumed to be between 1keV and 5keV. Without the proper calibration equipment more accurate estimates could not be provided.

Qualitatively however, the results show a marked production of high energy photons associated with the discharge.

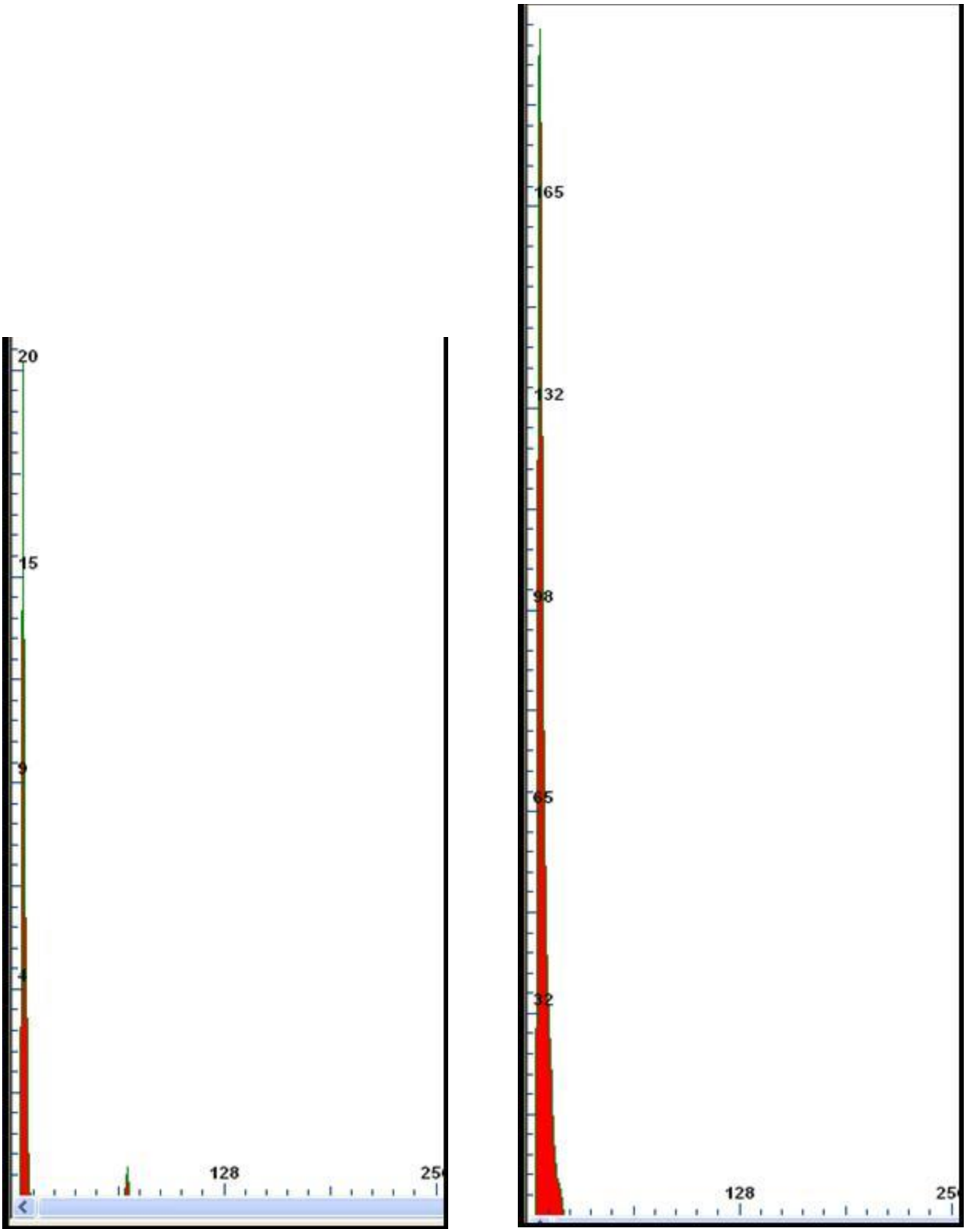


Figure 11: Left - Spectrum with Discharge OFF; Right - Spectrum with Discharge ON.

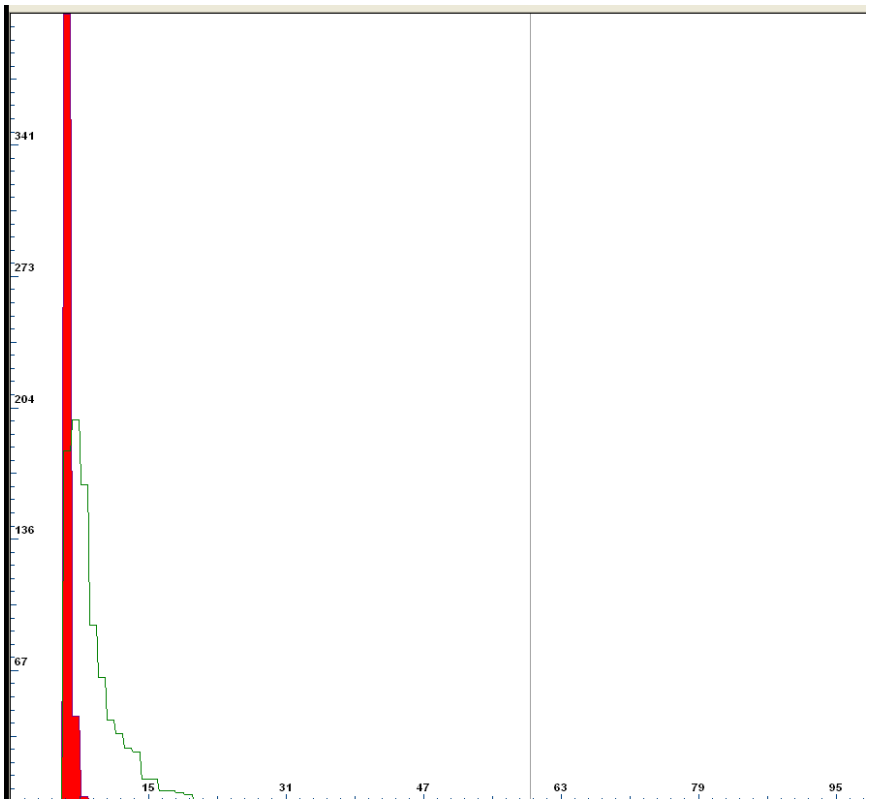


Figure 12: Zoomed in plot showing comparison between high energy radiation detected with discharge ON and OFF. The green line is the profile of the detected spectrum with the discharge ON. The intensity scales have been changed to fit the curves on the same plot.

Task 3. Plasma diagnostics using optical emission spectroscopy

The observed emission in the discharge can be considered as relaxation of some specific electronically excited species in the plasma. Thus identification of the wavelengths being emitted, as well as consideration of the liquid under investigation, would give information about the nature of the emitting species in the discharge.

The high voltage pulses delivered to the electrodes were supplied from the power supply via 50ft of coaxial cable. While reflections on the line could be isolated, for these experiments they could not be suppressed and thus associated with each "pulse" were multiple reflections due to ringing on the line. Energy dissipation in the discharge is low, and transmission line losses are also low, thus reflected pulses had amplitudes up to 5kV even after 5 reflections. These reflected pulses also initiated discharges subsequent to the first incident pulse, also producing significant emission. The interesting phenomenon in this work only involved studying the effect of the first incident pulse where the polarity of the anode (pin) was positive and the liquid was not immediately previously ionized. Careful analysis of the delays associated with the experimental setup and synchronization with the spectrometer detector allowed a time-resolved study of the discharge to be performed for only the first incident pulse; all subsequent emission from breakdown induced by reflected pulses were isolated.

All spectra were intensity corrected to accommodate for the non-uniformity in the spectral response of the camera, and background subtraction was performed throughout the experiments to improve the signal to noise ratio.

The duration of the voltage pulse in these experiments was 10ns at 90% maximum but emission on the rising and falling edge of the pulse as shown in Figure 6 meant that the emission phase associated with a single pulse lasted for 15ns. The detector was gated for 20ns over the duration of the first pulse, encompassing all the emission throughout the various phases, including the first stroke and the second stroke. This integrated spectrum is shown in Figure 13. The maximum of the spectrum peaks at 470nm, but without a clear, sharp apex. Thus, one can assume significant broadening and spectral line overlap leading to the observed shape in Figure 13. The peak resides between hydrogen wavelengths from the Balmer series: 486nm $H-\beta$ and 434nm $H-\gamma$. The peak also lies in the vicinity of atomic oxygen II with a wide range of emission lines between 467 and 475nm.

This integrated spectrum clearly contains information from the various emission phases identified in figure 6. A time resolved study was then used to dissect the spectrum over the lifetime of the various emission phases. The camera detector was gated for 3ns and spectra were captured over 2.8ns steps across the duration of the pulse. These results are shown in Figure 14.

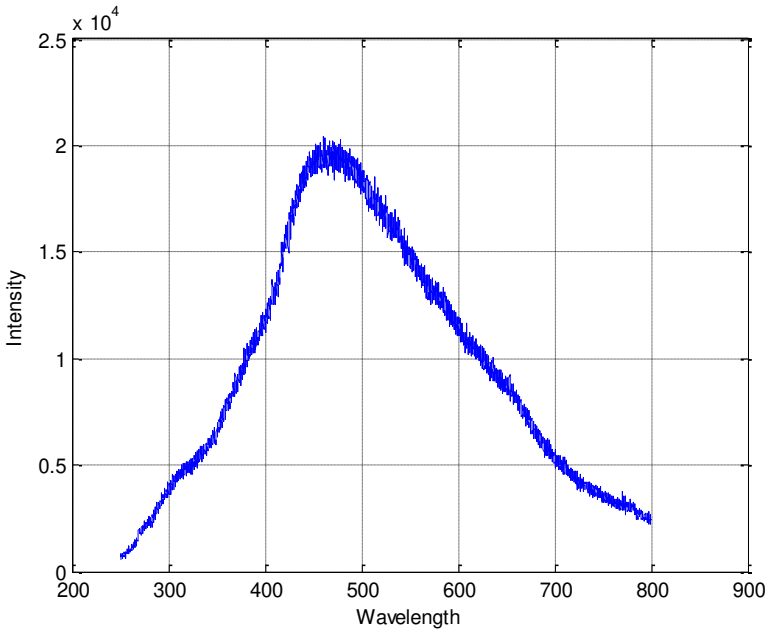


Figure 13: Integrated spectrum over duration of entire voltage pulse.

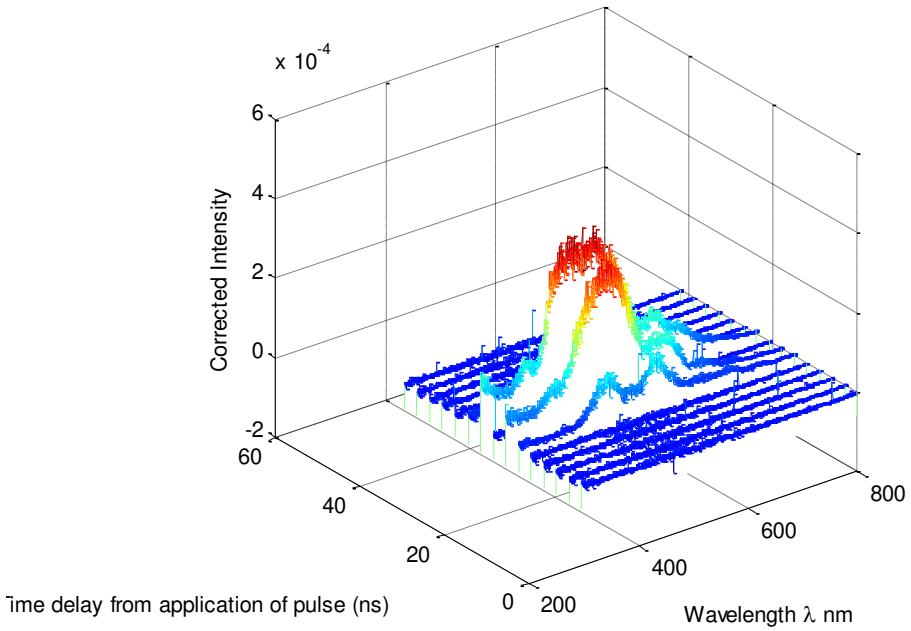


Figure 14: Waterfall plot showing evolution of the emission spectrum over time. All spectrum are taken with a 3ns gate in steps of 2.8ns

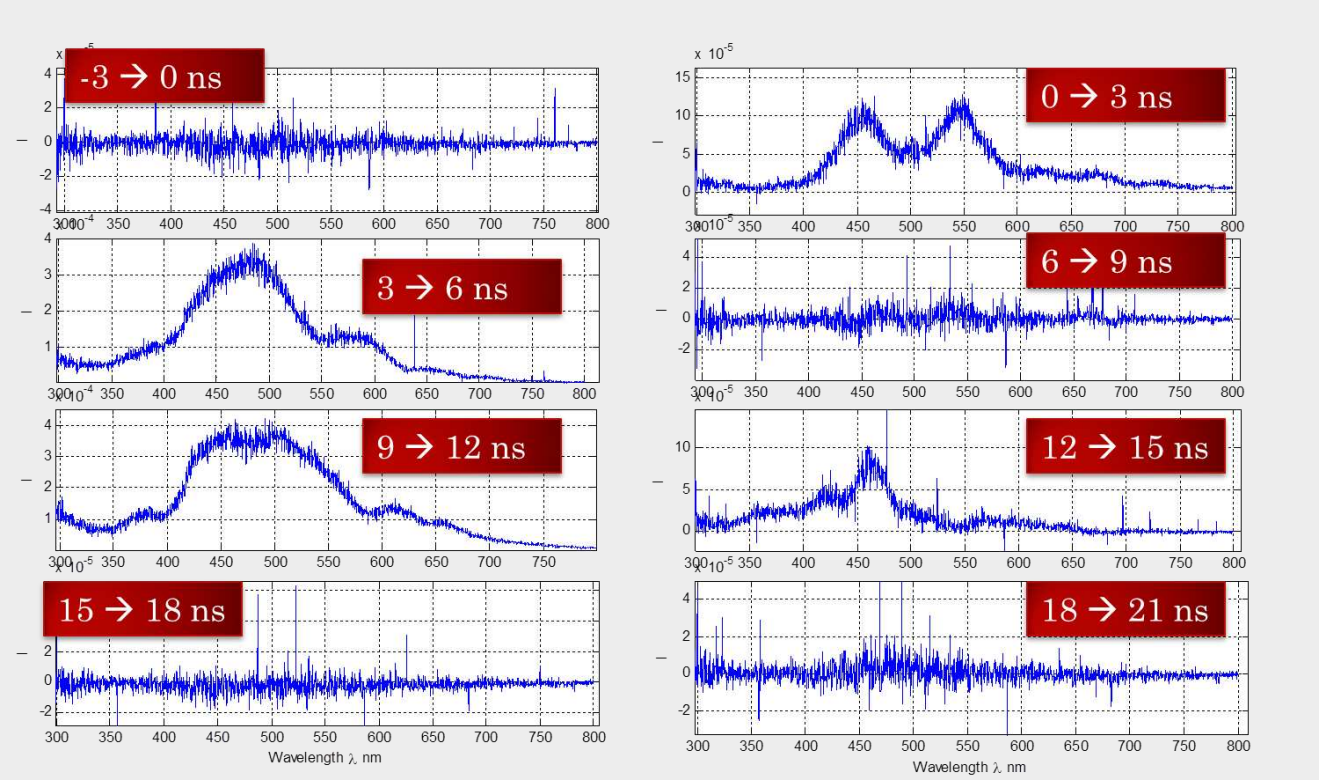


Figure 15: Evolution of the emission spectrum over the duration of the first pulse.

The decomposition of the spectrum is consistent with the discharge profile observed in Figure 6. From 6-9 ns the dark phase appears, coinciding with the dark phase seen during the voltage plateau. The spectral profile shows the dynamic nature of the emitting species over of the lifetime of the discharge.

The discharge spectrum integrated over 1 s (Figure 16) shows a strong broadening of Balmer lines with almost continuum emission in the region 300-900 nm and weak broadened OI lines. In order to estimate the discharge parameters, namely electron density and electron temperature, we have examined the Hα and OI (777 nm) profiles in detail. The best fit was obtained as a sum of two lorentzian functions (Figure 17). Since Stark and pressure broadening can be treated independently and both have lorentzian profile, one may suggest that complex Hα and OI profiles are due to the combined contribution of Van Der Waals and Stark broadening. It is important to mention, that Van Der Waals broadening is characterized by the line shift in red region $\Delta\lambda_{shift} \approx \frac{\Delta\lambda_{1/2}}{2.75}$, and the corresponding values for fitted lorenzian profile is in a good agreement with this value. Using Stark broadening parameters from Griem tables for Hα and OI and corresponding HWFM equations:

$$N_e = C(N_e, T)\Delta\lambda_S^{3/2}$$
$$\Delta\lambda = 2 \times 10^{-17}\omega_{tab}n_e\left[1 + 5.53 \times 10^{-6}A_{tab}n_e^{\frac{1}{4}}(1 - 0.75R(T_e))\right], \quad (2)$$

we have obtained graphs for electron densities as a function of electron temperature. We estimate electron density and electron temperature of the discharge as ~2×10^{17} cm^{-3} and ~6 eV respectively (Figure 18). This gives us an estimated value of Debye radius of ~50 nm and of Coulomb logarithm of ~6.

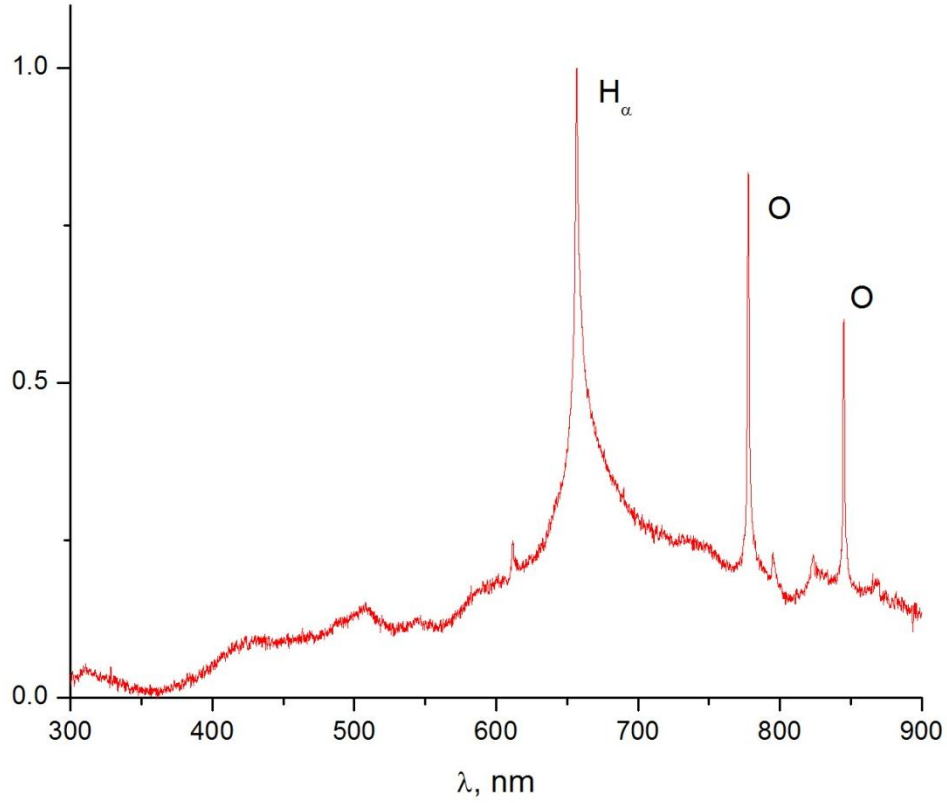


Figure 16 Spectrum of nanosecond discharge in liuqid water.

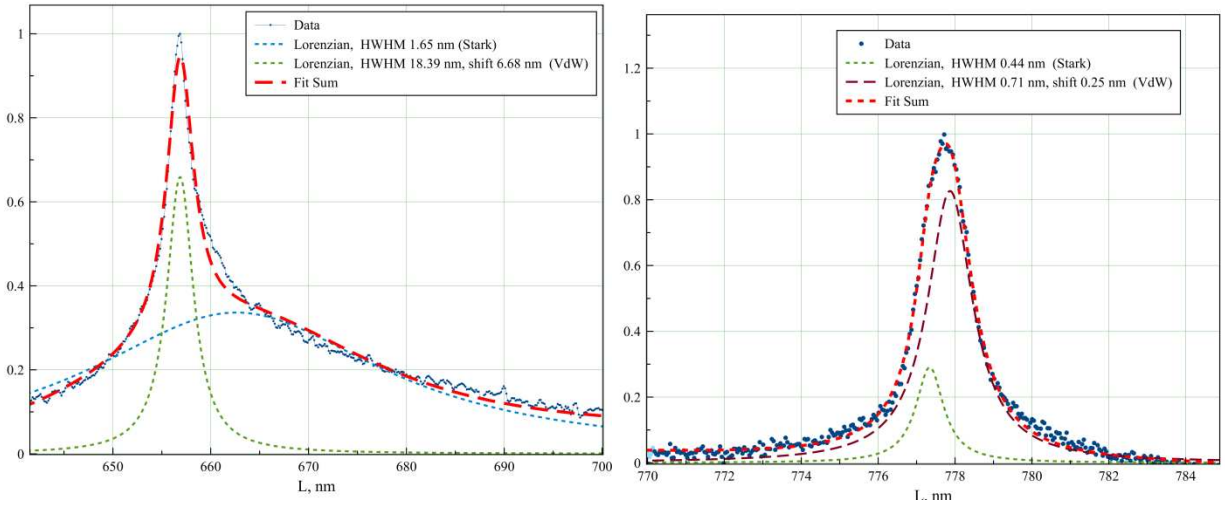


Figure 17 Hα and OI (777 nm) lines fitting by two lorenzian functions.

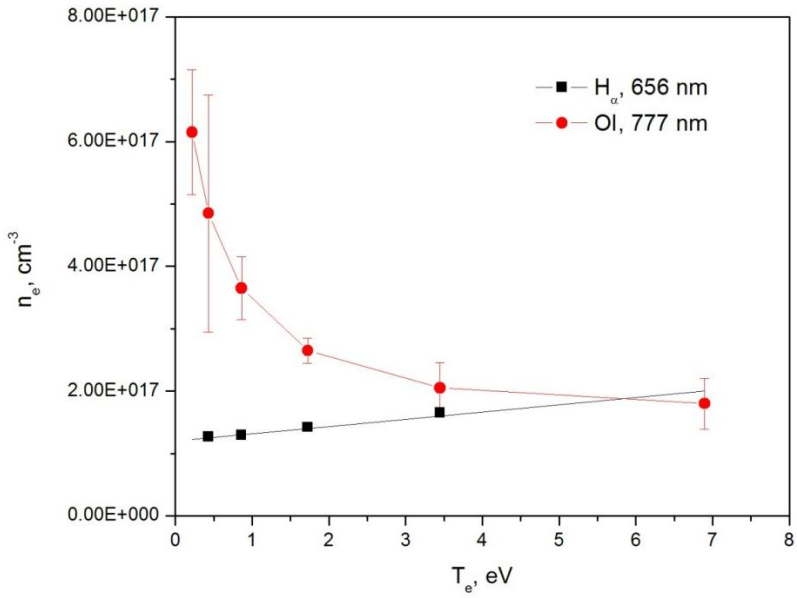


Figure 18 To the estimation of electron density and electron temperature

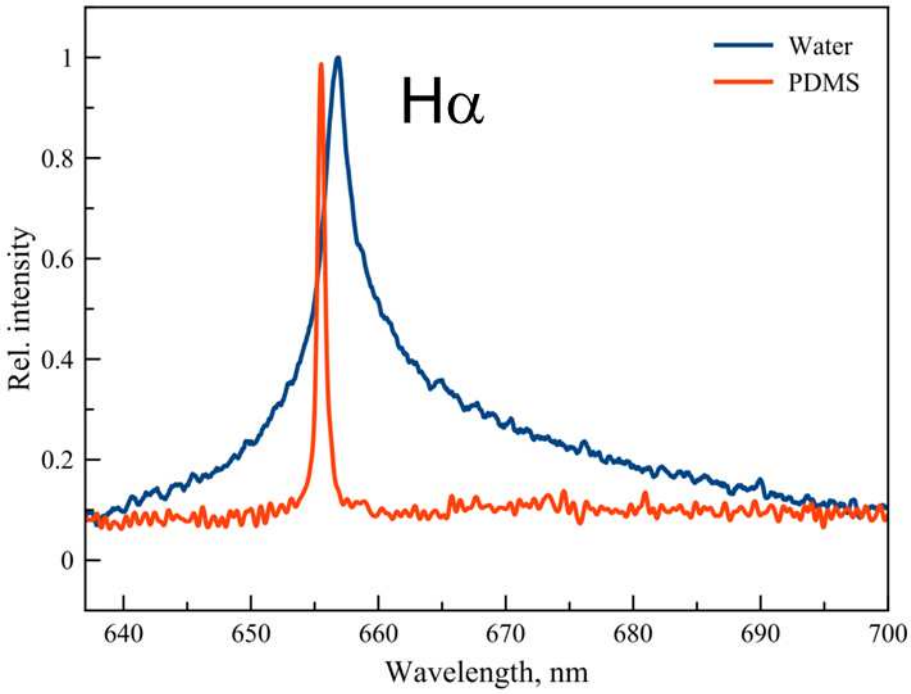


Figure 19 Comparison of the hydrogen alpha line width for the discharge in water and PDMS oil.

Comparing the spectra of the discharge ignited in water and oil, and using the same technique for determination of electron density, we show this value is 2 orders of magnitude lower for the case of PDMS: ne $\approx 10^{15}$ cm^{-3} (Figure 19 Comparison of the hydrogen alpha line width for the discharge in water and PDMS oil.).

Task 4. Effects of electrode size and material and externally applied electric and magnetic fields

The influence of the electrode properties were investigated using 2 different electrodes: a stainless steel needle with a 20μm radius of curvature tip, and an Iridium microprobe with a 1μm radius of curvature tip. Variation in the discharge gap and applied voltage was also performed and shown previously in Figure 8, Figure 9 and Figure 10. These results highlight the strong dependence on the local electric field near the tip, and not the globally applied voltage.

A point-to-plane electrode configuration has the advantage of being able to generate a very high, non-uniform electric field near the point electrode. The electric field intensity near the tip of the point electrode can be fairly accurately estimated by the formula:

$$E = \frac{2V}{r log\left(\frac{4d}{r}\right)}$$

Here, E is the electric field intensity (V/m); V is the applied voltage on the electrode gap (V); r is the radius of curvature of the electrode tip (m); and d is the electrode separation (m). Throughout these experiments, the applied voltages were varied from 11.2 to 15.5kV, with electrode gap separation from 1.3 to 6.5mm. Under these conditions, the estimated electric field near the electrode tip was varied between $5 - 60 MV\ cm^{-1}$. The inverse dependence of electric field on distance away from the tip however meant that these high electric fields only existed in extreme proximity of the electrode tip, as shown in Figure 20. The assumed parameters in this model were: $r = 5\mu m; d = 3mm;\ V = 31kV$.

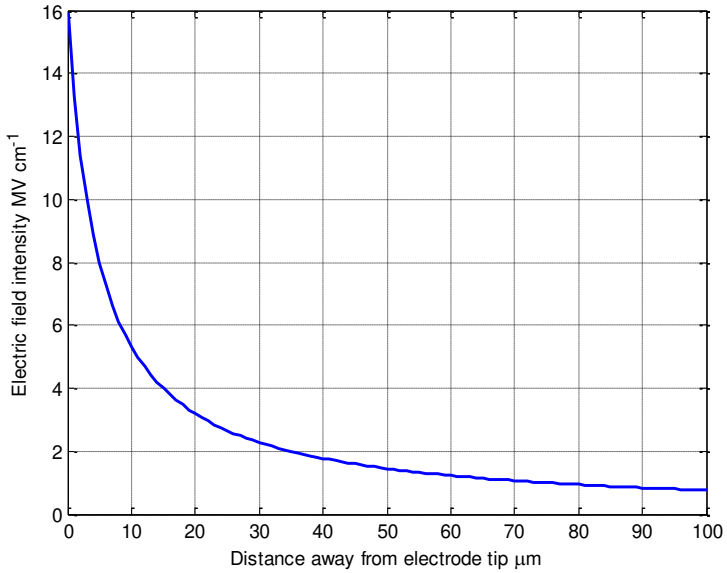


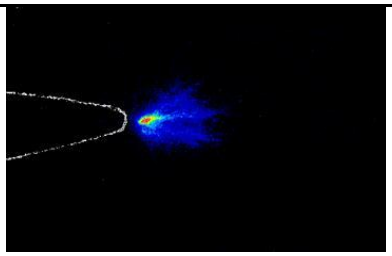
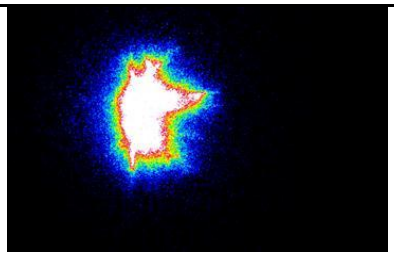
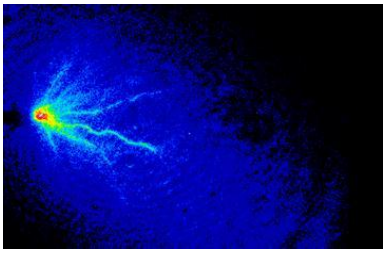
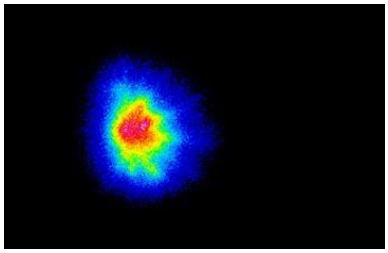
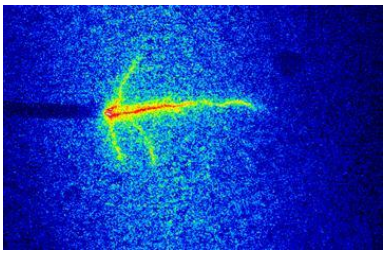
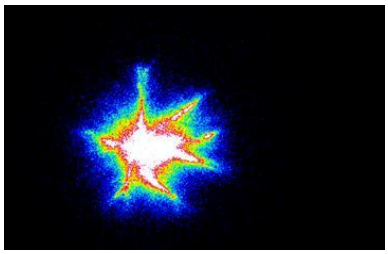
Figure 20: Electric field intensity as a function of distance away from point electrode tip.

From Figure 20 it can be seen that as close as 100μm away from the electrode tip, the electric field in drops sharply to below $1MV\ cm^{-1}$. Evidence in Figure 8 and Figure 9 though show that the discharge grows much large than this, growing to as much as 2mm. The external electric field in this region is not sufficient to sustain breakdown in these regions, so these discharge filaments must be propagating via their own electric field. This can be explained by the familiar streamer propagation in liquids mechanism that has been studied for many years.

We found that the size of the discharge is related to the applied external electric field, based on the images shown in Figure 8, Figure 9 and Figure 10. The strong dependence on the applied voltage rather than the electrode separation arises out of the high asymmetric geometry being used. Electrode separation d has a logarithmic influence on the local electric field, and hence only barely affects the local electric field.

The results summarizing the effect of the electrode material and radius of curvature along liquid properties is shown in Table 1 below. From the first and second row of results, we see little dependence of discharge structure and morphology for different electrodes and radius of curvature. This suggests that the initiation mechanism only requires sufficiently high local electric field, and is insensitive to the composition of the electrode providing the electric field concentration at the tip.

Table 1: Integral discharge images with exposure time of 50 ns obtained for different discharge gaps and electrodes for the cases of water and silicon transformer oil (PDMS)

	Silicon oil (PDMS, ε~2)	Distilled deionized water (ε~80)
Electrode radius 20 μm Discharge gap 1.8 mm		
Electrode radius 5 μm Discharge gap 1.8 mm		
Electrode radius 5 μm Discharge gap 3 mm		

Effect of external magnetic fields and electric fields

To investigate the effect of externally applied magnetic fields on the discharge development and structure, the discharge chamber was modified to include a probe with a 4T Neodymium magnet attached to the tip, the schematic of which is shown in Figure 21. The probe was positioned ~5mm from the tip of the anode, providing a magnetic field in the proximity of the discharge region of approximately 2 – 4 T. Experiments were performed with an applied voltage pulse of 15.5kV with an electrode separation of 7mm. Images of the emission were then taken to compare the presence and absence of the magnetic field and summarized in Figure 22 below. ICCD images were captured of the discharge for a single pulse, with 50 accumulations and also for 3ns at the beginning of the applied voltage when the first emission was seen. All results indicated no effect of the externally applied magnetic field.

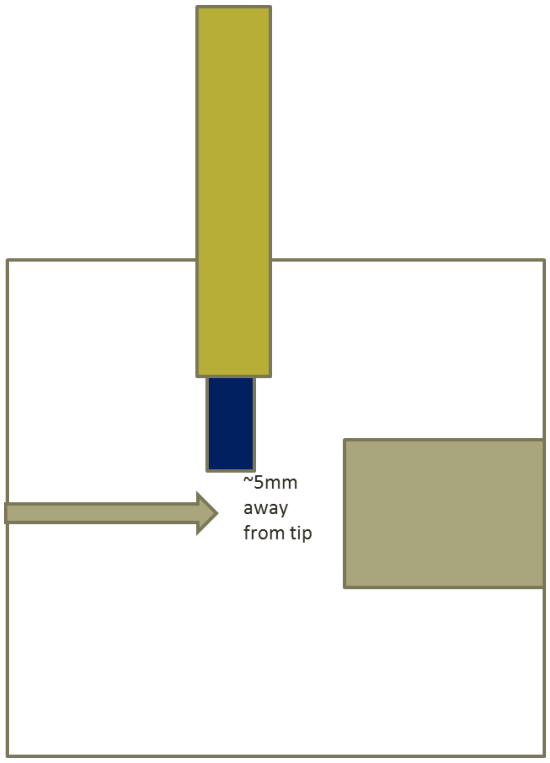


Figure 21: Schematic of apparatus to investigate B-Field effects on discharge.

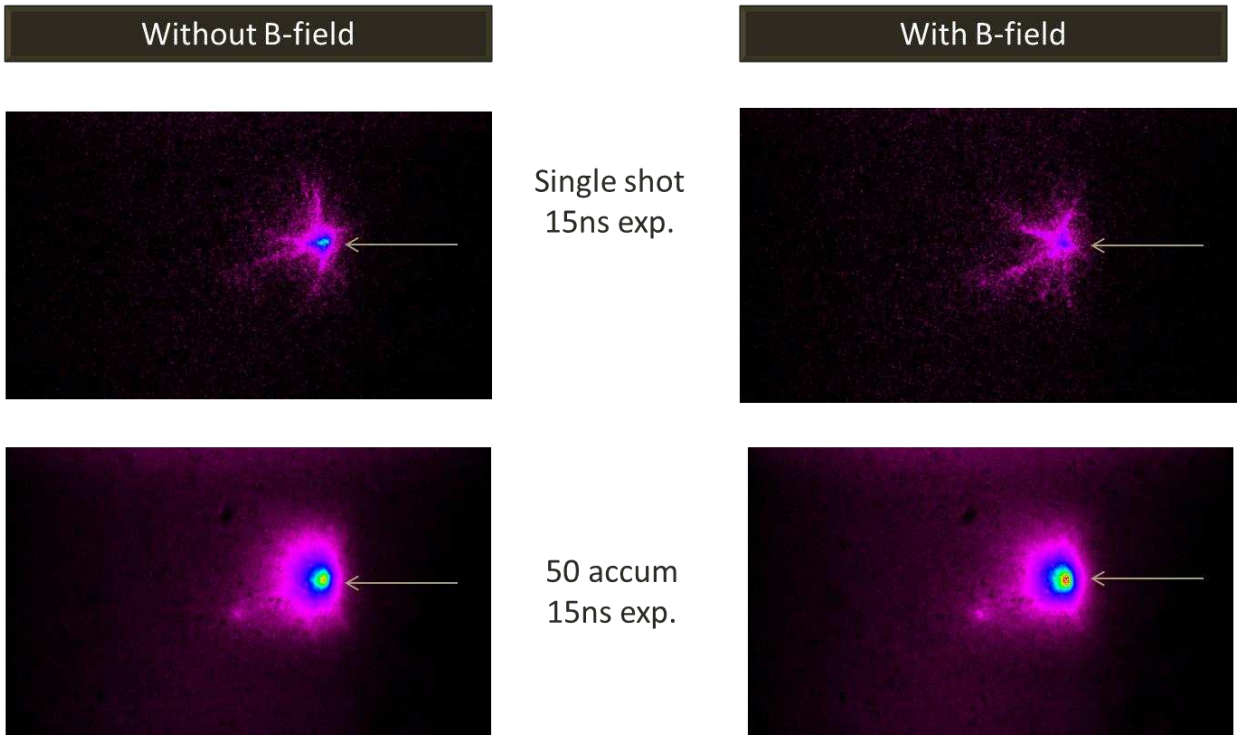


Figure 22: Effect of externally applied magnetic field. The top row shows the emission from the entire discharge lifetime for a single pulse. The bottom row shows an integrated accumulation from 50 pulses.

Experiments were also performed to investigate the effect of an externally applied electric field on the discharge. A similar modification to the discharge cell was made for these experiments and the schematic is shown in Figure 23. A quartz tube filled with copper paste was used as an insulated electrode and voltages up to -20kV DC was applied between this electrode and the walls of the chamber. The maximum estimated electric field existing on the region of the discharge was 5kV/cm. Similar electrical parameters and diagnostics were employed as in the experiments with the external magnetic field and the results summarized in Figure 24 below. ICCD images were captured for single pulses, 50 accumulations and for 3ns during the initial stage of the discharge. All results showed no effect on the discharge structure or development for the configuration and electric fields investigated in these experiments.

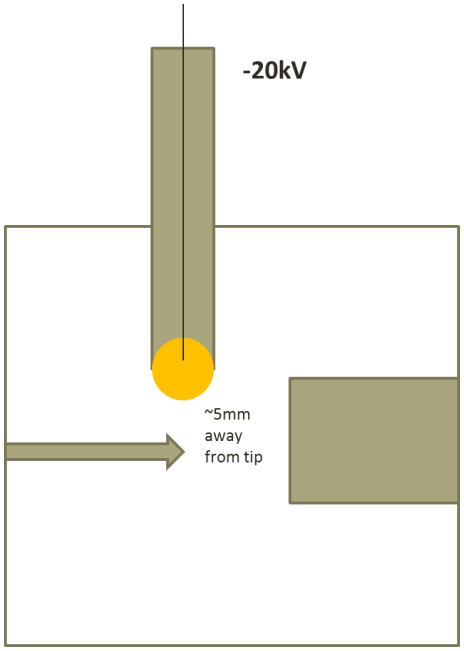


Figure 23: Schematic of apparatus to investigate E-Field effects on discharge.

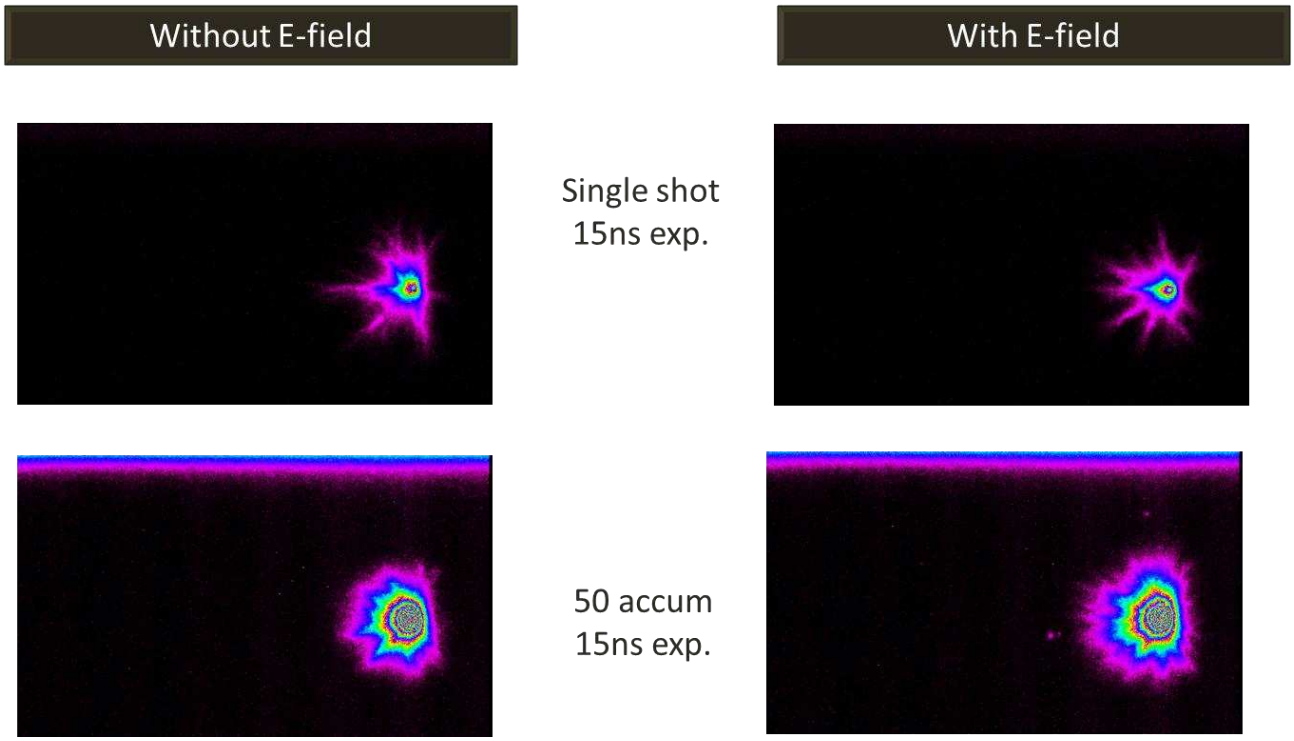


Figure 24: Effect of externally applied electric field ~ 5kV/cm. The top row shows the emission from the entire discharge lifetime for a single pulse. The bottom row shows an integrated accumulation from 50 pulses.

Task 5. Development of the discharge model

It is known that any dielectric, placed in non-uniform electric field, is affected by the volumetric ponderomotive (electrostrictive) forces, which tend to deform the dielectric and move it to the region of stronger field. Deformation due to the electrostrictive effect is caused by rearrangement of the orientation of the elementary dipoles and occurs over a time much shorter than the characteristic time of the hydrodynamic processes. It follows that there is a possibility of formation of discharge in the liquids in time scales much shorter than the formation time for bubbles near the electrode.

We consider pre-breakdown phenomena developing around a needle-like high voltage electrode, with a typical radius of curvature r_0 ~ 0.01- 0.1mm. The volumetric force acting on a dielectric fluid in nonuniform electric field determined by the Helmholtz equation:

$$\vec{F} = e\delta n\vec{E} - \frac{\varepsilon_0}{2}E^2\nabla\varepsilon + \frac{\varepsilon_0}{2}\nabla\left(E^2\frac{\partial\varepsilon}{\partial\rho}\rho\right), \qquad (1)$$

where the first term is the force acting on non-neutral fluid with free charges density $e\delta n$, the second and third terms are volumetric density of the ponderomotive forces, ε_0 is the vacuum dielectric permittivity, ρ is the liquid density, $\vec{E}$ is electric field. The 2nd term in (1) is associated with force acting on an inhomogeneous dielectric, and the third term corresponds to the electrostrictive forces in a non-uniform electric field associated with the tensions within the dielectric.

In the absence of breakdown we can neglect with the force acting on the free charges and with the inhomogeneity of the liquid. In this case, the body force acting on the liquid dielectric is reduced to

$$\vec{F} \approx \frac{\varepsilon_0}{2}\nabla\left(E^2\frac{\partial\varepsilon}{\partial\rho}\rho\right) \approx \frac{\varepsilon_0}{2}\left(\frac{\partial\varepsilon}{\partial\rho}\rho\right)\nabla E^2 \qquad (2)$$

where for nonpolar dielectrics, as follows from the Clausius-Mosotti formula:

$$\frac{\partial\varepsilon}{\partial\rho}\rho = \frac{(\varepsilon-1)\cdot(\varepsilon+1)}{3} \qquad (3)$$

and for polar dielectrics (water)

$$\frac{\partial\varepsilon}{\partial\rho}\rho = \alpha\varepsilon \qquad (3')$$

where $\alpha \le 1.5$ is the empirical factor for most of the studied polar dielectric liquids, including water.

The stretching internal stresses in the fluid, which are associated with the action of the volumetric forces (1) or (2), can lead to micro ruptures (cavitation) in the liquid. In accordance with the nucleation theory, the critical tension for the liquid rupture is given by:

$$p_c = p_{sat} - \left(\frac{16\pi\sigma^3}{3kT\ln(NB/J)} \right), \tag{4}$$

Here p_{sat} is the vapor pressure of liquid at a given temperature T, k is the Boltzmann constant, σ is the surface tension coefficient, J is the nucleation rate equal to the density of vapor bubbles of a critical size appearing per 1 second, $B = 10^{11}$ s is the kinetic coefficient which weakly dependent on temperature, and N is the density of molecules of the fluid. In practice the experimental limit stretching tension is much smaller than that predicted by the theory of homogeneous nucleation (equation (4)). Experiments show that at initially normal conditions (room temperature and atmospheric pressure) water ruptures at a negative pressure of about 0.15 MPa while slowly stretching. However, at the rapid stretching water preserves continuity for negative pressures up to higher orders. Measurements of p_c depend on many parameters, including the degree of purity of the fluid and the presence of dissolved gases and dust particles. Experimental data for water are in the range between ~6 and 50 Mpa.

We study the dynamics of dielectric liquid in a pulsed inhomogeneous electric field in the approximation of compressible fluid dynamics. We are looking for the numerical solution within the standard system of equations of continuity of mass and momentum.

$$\frac{\partial\rho}{\partial t} + \nabla(\rho\vec{u}) = 0 \tag{5}$$

$$\rho\left(\frac{\partial\vec{u}}{\partial t} + (\vec{u}\cdot\nabla)\vec{u} \right) = -\nabla p + \vec{F} + \eta_d\left(\Delta\vec{u} + \tfrac{1}{3}\nabla(\nabla\cdot\vec{u})\right) \tag{6}$$

and the Tait equation of state for "compressible" water:

$$p = (p_0 + B)\left(\frac{\rho}{\rho_0} \right)^{\gamma} - B \tag{7}$$

$\rho_0 = 1000$ kg/m^3, $p_0 = 10^5$ Pa, $B = 3.07\cdot 10^8$ Pa, $\gamma = 7.5$

Here ρ is the fluid density, p is the pressure, $\vec{u}$ is the velocity, η_d is the dynamic viscosity. Body force in (6) acting on the polar fluid is given by (2), (3')

$$\vec{F} = \frac{\varepsilon_0}{2}\nabla\left(E^2\frac{\partial\varepsilon}{\partial\rho}\rho \right) \approx \frac{\alpha\varepsilon_0}{2}\nabla E^2 \tag{8}$$

Due to the gradient form of the ponderomotive force (8), it is convenient to write (6) as

$$-\nabla p + \vec{F} = -\nabla\left(p - \frac{1}{2}\left(\frac{\partial \varepsilon}{\partial \rho}\rho\right)\varepsilon_0 E^2 \right). \qquad (9)$$

That is, as already noted, the ponderomotive electrostriction force is reduced to a negative pressure, stretching the liquid. Heating of fluid is neglected, since the change in kinetic energy during the pulse on orders smaller than its internal energy.

For the time scales of the order of tens of nanoseconds, the boundary layer d is much smaller than the radius of the electrode's tip, $r_{el} \sim 1-10$ μm, (the characteristic size of the electric field in the fluid), i.e. $d \approx \sqrt{\nu t} \approx 10^{-7}$ m $<< r_{el}$, where $\nu = \eta_d / \rho$ is the kinematic viscosity. For water at T = 293 K: $\eta_d \approx 10^{-3}$ Pa·s; $\nu \approx 10^{-6}$ m^2/s. The characteristic time in which the boundary layer is established, whose size is comparable to the radius of curvature of the electrode, r_{el}: $\tau \approx r_{el}^2 / \nu = 10^{-6} - 10^{-4}$ sec, ie by 2-4 orders longer than the front rise time for the high-voltage pulse at the electrode. Therefore, the terms related to the viscosity can be neglected in equation (6).

Since we consider processes in highly inhomogeneous field in the vicinity of a sharp needle electrode, which can be represented as a prolate ellipsoid, it is convenient to solve the equations for compressible fluid in prolate spheroidal coordinates , η, μ. In this case, the equipotential surfaces Φ coincide with surfaces $\eta = const$.

$$\Phi(\eta) = \Phi_0 \frac{\ln(\coth(0.5\eta))}{\ln(\coth(0.5\eta_0))} \qquad (10)$$

Here, $\Phi_0 = U(t)$ is the potential on the electrode, the value $\eta_0 = a \cdot \coth(\xi)$ corresponds to an equipotential surface which coincides with the electrode; ξ is the ratio of the semiaxes of the prolate ellipsoidal electrode;

$$a = r_{el}\cosh(\eta_0)/\sinh^2(\eta_0) \qquad (12)$$

is the focal distance, r_{el} is the radius of curvature of the electrode tip.

The relations linking the cylindrical coordinates with the prolate spheroidal coordinates in the axisymmetric case are as follows

$$\begin{aligned} r &= a \cdot \mathrm{sh}(\eta) \cdot \sin(\mu) \\ z &= a \cdot \mathrm{ch}(\eta) \cdot \cos(\mu) \\ \eta_0 &\le \eta < \infty \\ 0 &\le \mu \le \pi/2 \end{aligned} \qquad (13)$$

The corresponding Jacobian linking the cylindrical coordinates with prolate spheroidal is:

$$H = \left| \frac{\partial(r,z)}{\partial(\eta,\mu)} \right| = a^2 \left(\cosh(\eta) - \cos^2(\mu) \right) \tag{14}$$

The electric field in the variables η, μ is directed only along the η axis and is equal to:

$$E_\eta = \frac{1}{\sqrt{H}} \frac{\partial \Phi}{\partial \eta} = \frac{1}{\sqrt{H}} \frac{\Phi_0}{\sinh(\eta) \ln\left(\coth\left(0.5\eta_0\right)\right)} \tag{15}$$

Results and Discussion

We consider the transition process in the fluid at a voltage is applied to the needle - plane electrode system. The following set of parameters were chosen in our calculations: dielectric permittivity $\varepsilon = 81$; $\alpha = 1.5$; a negative pressure threshold at which cavitation starts, -30 MPa; the radius of the electrode tip, $r_{el} = 5$ μm; the eksintrisitet eksintrisitet (the ratio of the major semiaxis of the prolate ellipsoid to the small semiaxis) $\xi = 4$.

In Figure 25 the geometry of the problem and the grid in the prolate spheroidal coordinates are presented.

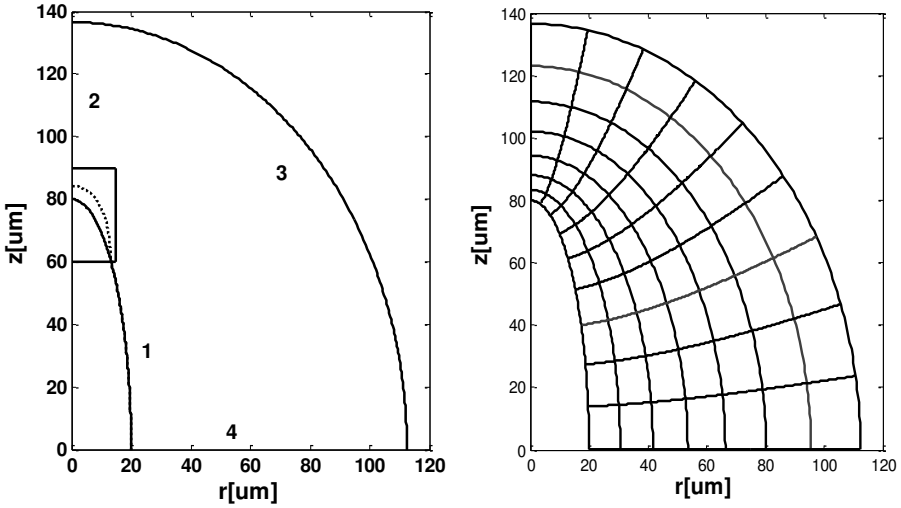


Figure 25. The boundaries of the area of integration of equations (5,6) and the grid in prolate spheroidal coordinates: 1 is the electrode surface, 2 is the symmetry axis, 3,4 are of the computational domain. For the area marked with rectangle the two-dimensional distributions of pressure and velocity in Figure 4 are shown. The dashed line shows schematically the region where the absolute value of the electrostrictive pressure exceeds the absolute value of the critical negative pressure necessary for cavitation.

In all computed cases a linear form of the voltage pulse $U(t) = U_0 t / t_0, t \le t_0$ was assumed. Here U_0 = 7 kV is the maximal voltage on the electrode, t_0 is the front duration. To study the effect of the voltage rise time, the calculations were performed for t_0=1, 5, 10 and 15 ns. A negative pressure in the fluid on

the symmetry axis (r= 0, z), caused by the electrostrictive forces at different moments of the voltage pulse is shown in Fig. 26.

Electrostrictive forces cause the fluid flow to the electrode. As a result, the absolute value of the total pressure in the fluid $|p_{tot}| = |p + p_E| < |p_E|$, $p_E = -0.5\alpha\varepsilon\varepsilon_0 E^2$. Thus at relatively shurp voltage pulse fronts, conditions arise for the development of cavitation, whereas cavitation under these conditions can not arise at more gentle pulse fronts. This is clearly demonstrating by the computed total pressure distributions on the symmetry axis at different times shown in Fig. 27 (A-D), where the dashed line shows the threshold pressure for cavitation.

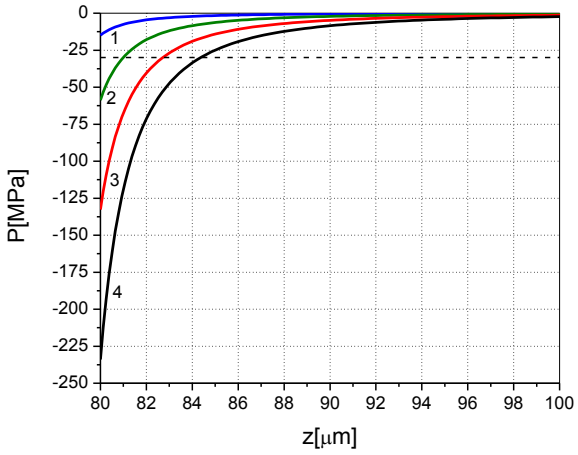


Figure 26**.** Electrostrictive negative pressure $p_E = -0.5\alpha\varepsilon\varepsilon_0 E^2$ in the fluid along the symmetry axis (r = 0, z) at the time moments: t/t_0 = 0.25 (curve 1); 0.5 (curve 2); 0.75 (curve 3) and 1 (curve 4). The dashed line shows the pressure threshold for cavitation when a rupture of continuity of fluid occurs.

In [10] was shown that the size of the area of the negative pressure where the conditions for the fluid cavitation raptures are fulfilled is proportional to the square of the amplitude of the applied voltage, and decreases in inversely proportion to the fourth power of the radius of the tip of the needle-like electrode. The performed calculations are in agreement with these qualitative regularities.

Velocity of the fluid flow arising under the considered conditions, during the entire voltage pulse remains subsonic and does not exceed tens of m/s (Fig. 27, middle column). Fluid influx to the electrode causes changes in density. However, in all computed cases, the maximum change in fluid density in the vicinity of the electrode does not exceed a few percent (Fig. 27, right column).

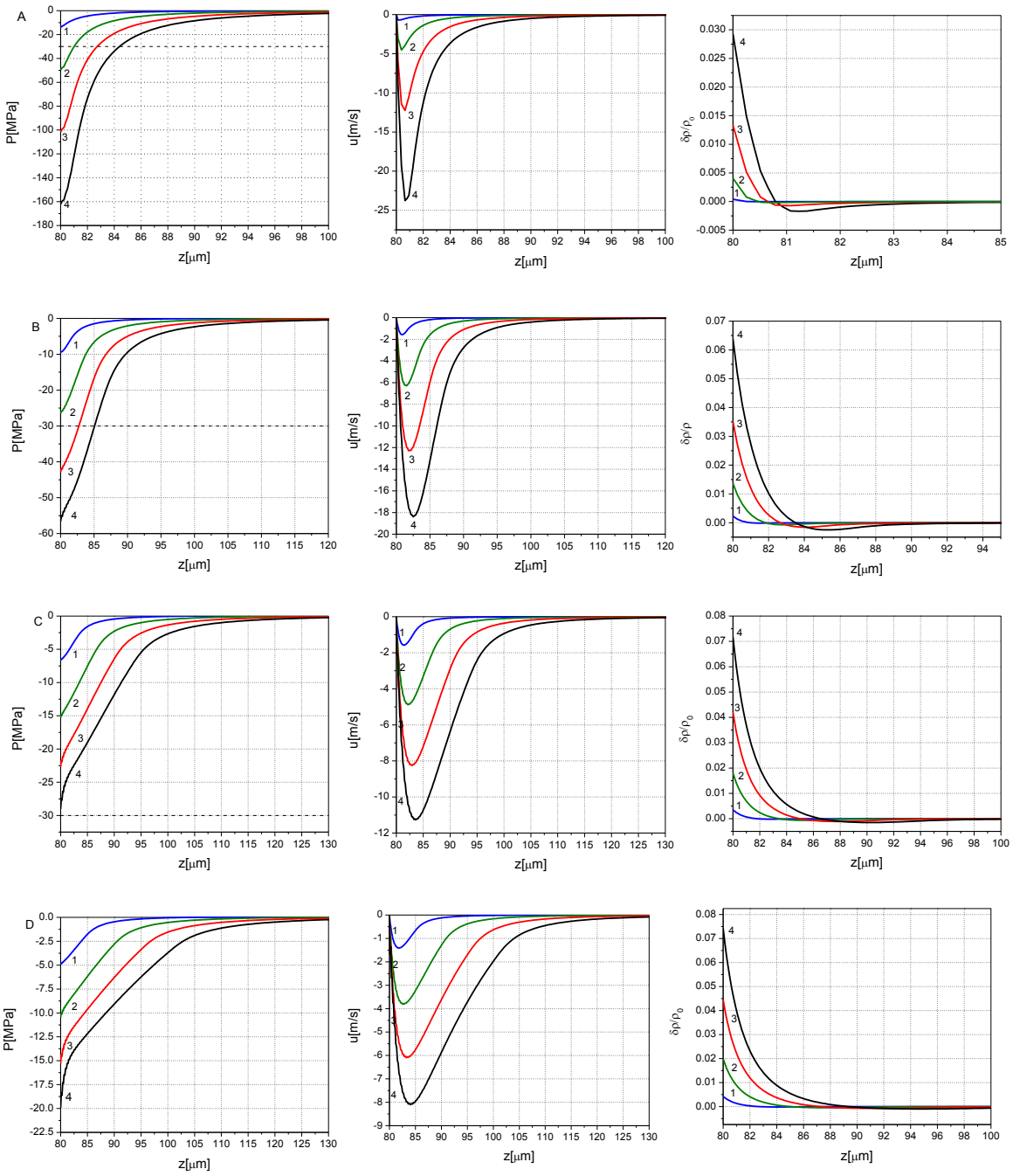


Figure 27 Longitudinal distributions of the total pressure p_{tot}; flow velocity u_z and relative density perturbation $\delta\rho/\rho_0$ along the symmetry axis (r=0, z). *A* – for the pulse with the rise time $t_0 = 1$ ns, *B* – $t_0 = 5$ ns, *C* - $t_0 = 10$ ns, *D* - $t_0 = 15$ ns. Curve 1 corresponds to the time moment $t/t_0 = 0.25$, 2 - $t/t_0 = 0.5$, 3 - $t/t_0 = 0.75$, 4 - $t/t_0 = 1$. The dashed line shows the pressure threshold for cavitation when a rupture of continuity of fluid occurs.

The obtained results show a qualitative difference between the behaviors of the liquid at a relatively fast or slow rise of a nonuniform electric field. At short rise time there are large tensile stresses (large negative

pressure), which can lead to discontinuities and cavitation formation of nanopores. At a relatively slow increasing of the field, the arising flow leads to a strong decreasing of the negative pressure up to values below the cavitation threshold and fluid ruptures not occurs.

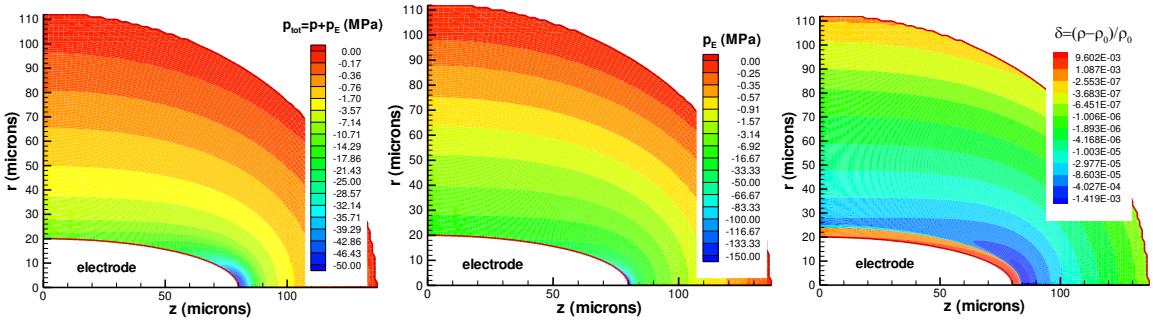


Figure 28. Contours of the total and ponderomotive pressures and the relative density perturbation at $t = 5ns$ for a pulse with a front duration t_0 = 5ns.

Figure 28 shows the contours of the total, p_{tot}, and ponderomotive, p_E, pressures and the relative density, $\delta = (\rho - \rho_0)/\rho_0$, at $t = 5ns$ for a pulse with a front duration t_0 = 5ns. The region of the electrode with the absolute value of negative pressures greater than 30 Mpa, where the conditions for the fluid rupture (formation of cavitation micropores) (left figure) is relatively small and extends in the vicinity of the electrode tip to the distance of order of 5 μm. The fluid density perturbation (right figure) is maximal in the vicinity of the electrode surface and then, a small region of rarefaction occurs due to fluid motion and stretching under the action of ponderomotive forces.

Note that for a dielectric fluid with a dielectric constant much lower than that of water, at the same electrode geometry and parameters of the voltage pulse cavitation ruptures cannot be formed because the tensile stresses determined by electrostriction force (8), are linearly dependent on the dielectric constant of the liquid.

5. Discussion and conclusions

Currently, there is no adequate model of the non-equilibrium discharge initiation in dense media - liquid. The reason for this is that liquid density is ~1000 times higher than that of gas phase, and this leads to much lower mean free path of electrons. Thus, for effective formation of a streamer in a liquid phase a much higher electric field is required (~30 MV/cm, [10]). A possible resolution to this problem is believed to be related to creation of local low density regions – bubbles or voids. The mechanisms by which these voids may be created have been proposed previously and are the following: (a) vaporization (Joule heating), (b) molecular decomposition, (c) mechanical movements, and (d) pre-existing micro-bubbles. In all these cases micro-bubbles grow with the speed equal to the speed of sound in liquid (~1 km/s), and if we assume that there is a void of a typical size of 1 μm created by the discharge or applied electric field in the liquid (as shown above, we have never observed any bubbles or voids in the experiment, where we could identify irregularities with the size of ~1 micron), its initial size 10 ns earlier (discharge initiation stage) should be only ~100 nm smaller. This raises another problem, namely – requirement for breakdown conditions inside of a small gas bubble or gas void. Considering that the bubble, if it already exists or is created by Joule heating or other mechanism, should be filled with a gas (vapor) at a pressure close to atmospheric pressure. In such a case, it is easy to estimate electric field that is required for breakdown and formation of an initial streamer from Meek's criterion: $\alpha d \geq 20$, where d – is a characteristic bubble size, $\alpha = pA\exp(\frac{B}{E/p})$ – Townsend coefficient, p – vapour (gas) pressure inside the bubble, A and B – are parameters for water vapor, and E is applied electric field. From this, one may notice that minimal size of a bubble that has to be present for formation of an initial streamer inside of it for the conditions of our experiments (applied electric field ~1-3 MV/cm) is on the order of 20 microns. The development of discharge inside of relatively large bubbles have been studied via numerical simulations elsewhere.

We propose a mechanism of the development of nanosecond non-equilibrium discharge in liquid phase without formation of bubbles based on the following:

1. *The discharge in water develops similarly to the discharges in long gaps – long sparks*. It is known, that breakdown mechanism based on multiplication of avalanches (Townsend mechanism) is predominant at low pd< 200 Torr cm, while at pd>4000 Torr cm, a streamer formation is considered as breakdown mechanism. The latter mechanism works only if the gap is not too long, the degree of electric field non-uniformity is not too high, and attachment is absent. In long gaps, although average electric field is low, *discharge develops by leader mechanism* – in the vicinity of point electrode, where electric field is the highest and conditions for formation of a streamer are fulfilled. Once a plasma channel is formed (because local electric field is sufficient for an avalanche-streamer transition), it grows due to high electric field of its charged tip. Similarly to the leader mechanism, the channel grows as long as leader propagation is sustained by the constantly rising applied electric field. A significant portion of the applied voltage drops on the plasma channel with finite conductivity. As a result, the field at the streamer head is not enough to maintain its propagation ("dark phase").
2. Let us now estimate a *criterion for a streamer formation in liquid phase without any voids or bubbles present.* Following classical theory of streamer formation, this would happen when the avalanche head electric field reaches value of the external electric field, i.e. electron number is

$$N_{e\,min} \sim \frac{4\pi\varepsilon_0 V_a d_s}{e} = \frac{4\pi\varepsilon_0 V_a \frac{V_a}{E_{ba}}}{e} \sim 2\times 10^8, \quad (3)$$

where V_a is the applied voltage (~30 kV), $d_s = 10\ \mu m$ is the distance which corresponds to the streamer formation electric field in a dense gas (E_{ba}~30 MV/cm). This number $N_{e\,min} \sim 2 \times 10^8$ that has to be produced in a 10 μm-radius volume is in a good agreement with experimentally observed electron density of $\sim 2 \times 10^{17}\ cm^{-3}$.

3. Minimum electron number that has to be generated for avalanche-to-streamer transition corresponds to the well-known *Meek's criterion*: $\alpha d \geq 20$. α^{-1} in this case has to be approximately $0.5\ \mu m$, which is unrealistically high for the conditions of highly condensed liquid media without any bubbles or voids present. In order to solve this problem, it is convenient to introduce another "ionization coefficient" μ that would represent effective electron multiplication inside of low-density region. Then, we may rewrite the Meek's criterion for liquid:
$$e^{\alpha d} \cdot e^{\mu d} \geq N_{e\,min}, \text{ or } (\alpha + \mu) d \geq 20. \quad (4)$$
4. Modified Meek's criterion may be represented by the following model. Let us imagine that highly inhomogeneous electric field in the vicinity of the high voltage electrode creates a number of *nano-sized pores* (ellipsoids elongated along the electric field lines) due to the so-called *ponderomotive electrostriction effect*: violation of the continuity of the liquid in the vicinity of the needle electrode due to the effective negative pressure which is a result of the electrostrictive ponderomotive force pushing dielectric fluid to the regions with higher electric field. This electrostrictive effect is caused by rearrangement of the orientation of the elementary dipoles and occurs over a time much shorter than the characteristic time of the hydrodynamic processes. It follows that there is a possibility of formation of discharge in the liquids in time scales much shorter than the formation time for bubbles near the electrode. We show that liquid in the vicinity of the electrode, $r < R$, where r – is the electrode radius and R is the radius of the region in which nanopores are created, is highly dispersed as a result of electrostriction, saturated by nanopores, and for the conditions of the experiments described above, we obtain $R \sim 1.9\, r_0$, where r_0 is the radius of the electrode (notice, that for the case of 5 μm radius electrode in the experiment, we have region radius $R \sim 10\ \mu m$). For our conditions we estimate pore size to be ~30 nm and corresponding energy that electron gains in the pore is ~100 eV. This energy is enough to cause ionization of liquid (ionization potential of water is ~12 eV) at the boundaries of nanopores, and to create several additional electrons. As we have shown above, effective "ionization coefficient" $\mu \sim 2 \times 10^4\ cm^{-1}$(assuming $\ll \mu$), which corresponds to a distance between nanopores of about ~500 nm. Thus, about 20 nanopores per 10 micron distance would be sufficient for a formation of an initial streamer. Sources of primary electrons in the cavities may include background radiation, negative ions (OH), as well as field emission from the surface of the cavities. Estimation of the electron emission from the surface of the pore calculated by the formulas Fowler-Nordheim for the tunneling of an electron from a hydrogen atom corrected on work function in a molecule of water, show that in a pore that is a sphere of diameter ~l, during time of ~ 1 ns in the pore appear more than one electron.
5. Thus, from our analysis, the scenario for pulsed nanosecond breakdown in liquid dielectrics may be proposed as follows. In the beginning, *strong inhomogeneous electric field at the needle electrode creates a region saturated by nanopores*. In these pores, primary electrons are accelerated by electric field to the energies exceeding the potential of ionization of water molecule. This causes formation of a *primary streamer in liquid phase according to the modified Meek's criterion* $(\alpha + \mu) d \geq 20$. After neutralization of electrons at the electrode, positive ions in liquid form a *virtual needle electrode*, and electrostrictive conditions for the appearance of the next set of cavities are fulfilled. This propagation of streamer continues until the drop of voltage on the moving streamer will not be an order of initial voltage on the needle electrode. In the process of propagation the head of streamer narrows, so that electrostrictive conditions for breakdown are reproduced in the vicinity of the streamer head. It has to be noted, that this breakdown mechanism of liquid dielectrics is valid only when the rise time of the electrode

potential τ_V is much shorter than time of equalizing the pressure in region of formation of pores $\tau_V << R / C_S$, where C_S is the speed of sound in a liquid.

6. Publications and conference proceedings

1. “On the initial stage of the sub-nanosecond pulsed breakdown in liquid dielectrics”, IEEE Transaction on Dielectrics and Electrical Insulation, 2012

2. “Analysis of Streamer Propagation for Electric Breakdown in Liquid/Bioliquid”, Plasma Medicine Journal, 1, 1, 2011

3. “Non-equilibrium nanosecond-pulsed plasma generation in liquid phase (water, PDMS) without bubbles: fast imaging, spectroscopy and leader-type model”, New Journal of Physics, 2012 (submitted)

Conference proceedings:

1. “Nanosecond Pulse Discharge in High Density Polymer Liquid (PDMS)”, ICOPS-2012, Scotland, UK

2. “Generation of Plasma in Liquid Without Bubbles by Nanosecond Pulsed Discharge: Fast Imaging and Modeling”, ICOPS-2012, Scotland, UK

7. References

[1] W. G. Graham and K. R. Stalder, "Plasmas in liquids and some of their applications in nanoscience," *Journal of Physics D: Applied Physics,* vol. 44, p. 174037, 2011.

[2] V. V. Lopatin*, et al.*, "Initiation and development of nanosecond discharges in liquids," *Russian Physics Journal,* vol. 18, pp. 376-381, 1975.

[3] P. H. Ceccato*, et al.*, "Time-resolved nanosecond imaging of the propagation of a corona-like plasma discharge in water at positive applied voltage polarity," *Journal of Physics D: Applied Physics,* vol. 43, p. 175202, 2010.

[4] A. A. Fridman and L. A. Kennedy, *Plasma physics and engineering*, 2nd ed. Boca Raton, FL: CRC Press, 2011.

[5] L. Bruggeman, "Non-thermal plasmas in and in contact with liquids," *Journal of Physics D: Applied Physics,* vol. 42, p. 28, 2009.

[6] A. Fridman*, et al.*, *Plasma Discharge in Liquid: Water Treatment and Applications*, 1 ed. vol. 1: CRC Press 2012, 2012.

[7] Y. Yang*, et al.*, "Plasma discharge in water and its application for industrial cooling water treatment," Ph D, Drexel University, Philadelphia, Pa., 2011.

[8] R. P. Joshi*, et al.*, "Aspects of Plasma in Water: Streamer Physics and Applications," *Plasma Processes and Polymers,* vol. 6, pp. 763-777, 2009.

[9] M. A. Malik*, et al.*, "Water purification by electrical discharges," *Plasma Sources Science and Technology,* vol. 10, Febuary 2001 2001.

[10] A. Starikovskiy*, et al.*, "Non-equilibrium plasma in liquid water: dynamics of generation and quenching," *Plasma Sources Science and Technology,* vol. 20, p. 024003, 2011.

[11] P. Ceccato, "Filamentary plasma discharge inside water: initiation and propagation of a plasma in a dense medium," Doctor, Physics, Ecole Polytechnique, Palaiseau Cedex, 2009.

[12] L. Schaper*, et al.*, "Plasma production in electrically conducting liquids," *Plasma Sources Science and Technology,* vol. 20, 11 April 2011 2011.

[13] E. M. Stuve, "Ionization of water in interfacial electric fields: An electrochemical view," *Chemical Physics Letters,* vol. 519–520, pp. 1-17, 2012.

[14] G. P. McCormick and E. Howells, "Arcing resistance of high fire point dielectric liquids," *Power Delivery, IEEE Transactions on,* vol. 12, pp. 1184-1192, 1997.

[15] K. Udagawa*, et al.*, "Experimental Study of a Fast Ionization Wave Discharge at High Pulse Repetition Rates," presented at the 46th Aerospace Sciences Meeting and Exhibit, Reno, NV, 2008.

[16] D. Staack*, et al.*, "Nanoscale Corona Discharge in Liquids, Enabling Nanosecond Optical Emission Spectroscopy," *Angewandte Chemie International Edition,* vol. 47, pp. 8020-8024, 2008.

[17] B. Locke and S. Thagard, "Analysis and Review of Chemical Reactions and Transport Processes in Pulsed Electrical Discharge Plasma Formed Directly in Liquid Water," *Plasma Chemistry and Plasma Processing,* vol. 32, pp. 875-917, 2012.